



ELSEVIER

Contents lists available at ScienceDirect

# Nuclear Instruments and Methods in Physics Research A

journal homepage: [www.elsevier.com/locate/nima](http://www.elsevier.com/locate/nima)

## The T2K experiment

K. Abe<sup>aw</sup>, N. Abgrall<sup>p</sup>, H. Aihara<sup>av</sup>, Y. Ajima<sup>r</sup>, J.B. Albert<sup>m</sup>, D. Allan<sup>au</sup>, P.-A. Amaudruz<sup>az</sup>, C. Andreopoulos<sup>au</sup>, B. Andrieu<sup>ak</sup>, M.D. Anerella<sup>f</sup>, C. Angelsen<sup>au</sup>, S. Aoki<sup>aa</sup>, O. Araoka<sup>r</sup>, J. Argyriades<sup>p</sup>, A. Ariga<sup>c</sup>, T. Ariga<sup>c</sup>, S. Assylbekov<sup>k</sup>, J.P.A.M. de André<sup>n</sup>, D. Autiero<sup>af</sup>, A. Badertscher<sup>o</sup>, O. Ballester<sup>s</sup>, M. Barbi<sup>an</sup>, G.J. Barker<sup>bd</sup>, P. Baron<sup>h</sup>, G. Barr<sup>aj</sup>, L. Bartoszek<sup>j</sup>, M. Batkiewicz<sup>q</sup>, F. Bay<sup>c</sup>, S. Bentham<sup>ac</sup>, V. Berardi<sup>v</sup>, B.E. Berger<sup>k</sup>, H. Berns<sup>be</sup>, I. Bertram<sup>ac</sup>, M. Besnier<sup>n</sup>, J. Beucher<sup>h</sup>, D. Beznosko<sup>ah</sup>, S. Bhadra<sup>bg</sup>, P. Birney<sup>ba,az</sup>, D. Bishop<sup>az</sup>, E. Blackmore<sup>az</sup>, F.d.M. Blaszczyk<sup>h</sup>, J. Blocki<sup>q</sup>, A. Blondel<sup>p</sup>, A. Bodek<sup>ao</sup>, C. Bojecho<sup>ba</sup>, J. Bouchez<sup>1</sup>, T. Boussuge<sup>h</sup>, S.B. Boyd<sup>bd</sup>, M. Boyer<sup>h</sup>, N. Braam<sup>ba</sup>, R. Bradford<sup>ao</sup>, A. Bravar<sup>p</sup>, K. Briggs<sup>bd</sup>, J.D. Brinson<sup>ae</sup>, C. Bronner<sup>n</sup>, D.G. Brook-Roberge<sup>e</sup>, M. Bryant<sup>e</sup>, N. Buchanan<sup>k</sup>, H. Budd<sup>ao</sup>, M. Cadabeschi<sup>ay</sup>, R.G. Calland<sup>ad</sup>, D. Calvet<sup>h</sup>, J. Caravaca Rodríguez<sup>s</sup>, J. Carroll<sup>ad</sup>, S.L. Cartwright<sup>ar</sup>, A. Carver<sup>bd</sup>, R. Castillo<sup>s</sup>, M.G. Catanesi<sup>v</sup>, C. Cavata<sup>h</sup>, A. Cazes<sup>af</sup>, A. Cervera<sup>t</sup>, J.P. Charrier<sup>h</sup>, C. Chavez<sup>ad</sup>, S. Choi<sup>aq</sup>, S. Chollet<sup>n</sup>, G. Christodoulou<sup>ad</sup>, P. Colas<sup>h</sup>, J. Coleman<sup>ad</sup>, W. Coleman<sup>ae</sup>, G. Collazuol<sup>x</sup>, K. Connolly<sup>be</sup>, P. Cooke<sup>ad</sup>, A. Curioni<sup>o</sup>, A. Dabrowska<sup>q</sup>, I. Danko<sup>al</sup>, R. Das<sup>k</sup>, G.S. Davies<sup>ac</sup>, S. Davis<sup>be</sup>, M. Day<sup>ao</sup>, X. De La Broise<sup>h</sup>, P. de Perio<sup>ay</sup>, G. De Rosa<sup>w</sup>, T. Dealtry<sup>aj,au</sup>, A. Debraine<sup>n</sup>, E. Delagnes<sup>h</sup>, A. Delbart<sup>h</sup>, C. Densham<sup>au</sup>, F. Di Lodovico<sup>am</sup>, S. Di Luise<sup>o</sup>, P. Dinh Tran<sup>n</sup>, J. Dobson<sup>u</sup>, J. Doornbos<sup>az</sup>, U. Dore<sup>y</sup>, O. Drapier<sup>n</sup>, F. Druillolle<sup>h</sup>, F. Dufour<sup>p</sup>, J. Dumarchez<sup>ak</sup>, T. Durkin<sup>au</sup>, S. Dytman<sup>al</sup>, M. Dziewiecki<sup>bc</sup>, M. Dziomba<sup>be</sup>, B. Ellison<sup>ae</sup>, S. Emery<sup>h</sup>, A. Ereditato<sup>c</sup>, J.E. Escallier<sup>f</sup>, L. Escudero<sup>t</sup>, L.S. Esposito<sup>o</sup>, W. Faszer<sup>az</sup>, M. Fechner<sup>m</sup>, A. Ferrero<sup>p</sup>, A. Finch<sup>ac</sup>, C. Fisher<sup>az</sup>, M. Fitton<sup>au</sup>, R. Flight<sup>ao</sup>, D. Forbush<sup>be</sup>, E. Frank<sup>c</sup>, K. Fransham<sup>ba</sup>, Y. Fujii<sup>r</sup>, Y. Fukuda<sup>ag</sup>, M. Gallop<sup>az</sup>, V. Galymov<sup>bg</sup>, G.L. Ganetis<sup>f</sup>, F.C. Gannaway<sup>am</sup>, A. Gaudin<sup>ba</sup>, J. Gaweda<sup>s</sup>, A. Gendotti<sup>o</sup>, M. George<sup>am</sup>, S. Giffin<sup>an</sup>, C. Giganti<sup>s,h</sup>, K. Gilje<sup>ah</sup>, I. Giomataris<sup>h</sup>, J. Giraud<sup>h</sup>, A.K. Ghosh<sup>f</sup>, T. Golan<sup>bf</sup>, M. Goldhaber<sup>1</sup>, J.J. Gomez-Cadenas<sup>t</sup>, S. Gomi<sup>ab</sup>, M. Gonin<sup>n</sup>, M. Goyette<sup>az</sup>, A. Grant<sup>at</sup>, N. Grant<sup>au</sup>, F. Grañena<sup>s</sup>, S. Greenwood<sup>u</sup>, P. Gumplinger<sup>az</sup>, P. Guzowski<sup>u</sup>, M.D. Haigh<sup>aj</sup>, K. Hamano<sup>az</sup>, C. Hansen<sup>t</sup>, T. Hara<sup>aa</sup>, P.F. Harrison<sup>bd</sup>, B. Hartfiel<sup>ae</sup>, M. Hartz<sup>bg,ay</sup>, T. Haruyama<sup>r</sup>, R. Hasanen<sup>ba</sup>, T. Hasegawa<sup>r</sup>, N.C. Hastings<sup>an</sup>, S. Hastings<sup>e</sup>, A. Hatzikoutelis<sup>ac</sup>, K. Hayashi<sup>r</sup>, Y. Hayato<sup>aw</sup>, T.D.J. Haycock<sup>ar</sup>, C. Hearty<sup>e,3</sup>, R.L. Helmer<sup>az</sup>, R. Henderson<sup>az</sup>, S. Herlant<sup>h</sup>, N. Higashi<sup>r</sup>, J. Hignight<sup>ah</sup>, K. Hiraide<sup>ab</sup>, E. Hirose<sup>r</sup>, J. Holeczek<sup>as</sup>, N. Honkanen<sup>ba</sup>, S. Horikawa<sup>o</sup>, A. Hyndman<sup>am</sup>, A.K. Ichikawa<sup>ab</sup>, K. Ieki<sup>ab</sup>, M. Ieva<sup>s</sup>, M. Iida<sup>r</sup>, M. Ikeda<sup>ab</sup>, J. Ilic<sup>au</sup>, J. Imber<sup>ah</sup>, T. Ishida<sup>r</sup>, C. Ishihara<sup>ax</sup>, T. Ishii<sup>r</sup>, S.J. Ives<sup>u</sup>, M. Iwasaki<sup>av</sup>, K. Iyogi<sup>aw</sup>, A. Izmaylov<sup>z</sup>, B. Jamieson<sup>e</sup>, R.A. Johnson<sup>j</sup>, K.K. Joo<sup>i</sup>, G. Jover-Manas<sup>s</sup>, C.K. Jung<sup>ah,\*</sup>, H. Kaji<sup>ax</sup>, T. Kajita<sup>ax</sup>, H. Kakuno<sup>av</sup>, J. Kameda<sup>aw</sup>, K. Kaneyuki<sup>1</sup>, D. Karlen<sup>ba,az</sup>, K. Kasami<sup>r</sup>, V. Kasey<sup>u</sup>, I. Kato<sup>az</sup>, H. Kawamuko<sup>ab</sup>, E. Kearns<sup>d</sup>, L. Kellet<sup>ad</sup>, M. Khabibullin<sup>z</sup>, M. Khaleeq<sup>u</sup>, N. Khan<sup>az</sup>, A. Khotjantsev<sup>z</sup>, D. Kielczewska<sup>bb</sup>, T. Kikawa<sup>ab</sup>, J.Y. Kim<sup>i</sup>, S.-B. Kim<sup>aq</sup>, N. Kimura<sup>r</sup>, B. Kirby<sup>e</sup>, J. Kisiel<sup>as</sup>, P. Kitching<sup>a</sup>, T. Kobayashi<sup>r</sup>, G. Kogan<sup>u</sup>, S. Koike<sup>r</sup>, T. Komorowski<sup>ac</sup>, A. Konaka<sup>az</sup>, L.L. Kormos<sup>ac</sup>, A. Korzenev<sup>p</sup>, K. Koseki<sup>r</sup>, Y. Koshio<sup>aw</sup>, Y. Kouzuma<sup>aw</sup>, K. Kowalik<sup>b</sup>, V. Kravtsov<sup>k</sup>, I. Kreslo<sup>c</sup>, W. Kropp<sup>g</sup>, H. Kubo<sup>ab</sup>, J. Kubota<sup>ab</sup>, Y. Kudenko<sup>z</sup>, N. Kulkarni<sup>ae</sup>, L. Kurchaninov<sup>az</sup>, Y. Kurimoto<sup>ab</sup>, R. Kurjata<sup>bc</sup>, Y. Kurosawa<sup>ab</sup>, T. Kutter<sup>ae</sup>, J. Lagoda<sup>b</sup>, K. Laihem<sup>ap</sup>, R. Langstaff<sup>ba,az</sup>, M. Laveder<sup>x</sup>, T.B. Lawson<sup>ar</sup>, P.T. Le<sup>ah</sup>, A. Le Coguie<sup>h</sup>, M. Le Ross<sup>az</sup>, K.P. Lee<sup>ax</sup>, M. Lenckowski<sup>ba,az</sup>, C. Licciardi<sup>an</sup>, I.T. Lim<sup>i</sup>, T. Lindner<sup>e</sup>, R.P. Litchfield<sup>bd,ab</sup>, A. Longhin<sup>h</sup>, G.D. Lopez<sup>ah</sup>, P. Lu<sup>e</sup>, L. Ludovici<sup>y</sup>, T. Lux<sup>s</sup>, M. Macaire<sup>h</sup>, L. Magaletti<sup>v</sup>, K. Mahn<sup>az</sup>, Y. Makida<sup>r</sup>, C.J. Malafis<sup>ah</sup>, M. Malek<sup>u</sup>, S. Manly<sup>ao</sup>, A. Marchionni<sup>o</sup>, C. Mark<sup>az</sup>, A.D. Marino<sup>j,ay</sup>, A.J. Marone<sup>f</sup>, J. Marteau<sup>af</sup>, J.F. Martin<sup>ay,3</sup>, T. Maruyama<sup>r</sup>, T. Maryon<sup>ac</sup>, J. Marzec<sup>bc</sup>, P. Masliah<sup>u</sup>, E.L. Mathie<sup>an</sup>, C. Matsumura<sup>ai</sup>, K. Matsuoka<sup>ab</sup>, V. Matveev<sup>z</sup>, K. Mavrokoridis<sup>ad</sup>, E. Mazzucato<sup>h</sup>, N. McCauley<sup>ad</sup>, K.S. McFarland<sup>ao</sup>, C. McGrew<sup>ah</sup>, T. McLachlan<sup>ax</sup>, I. Mercer<sup>ac</sup>, M. Messina<sup>c</sup>, W. Metcalf<sup>ae</sup>, C. Metelko<sup>au</sup>, M. Mezzetto<sup>x</sup>

P. Mijakowski<sup>b</sup>, C.A. Miller<sup>az</sup>, A. Minamino<sup>ab</sup>, O. Mineev<sup>z</sup>, S. Mine<sup>g</sup>, R.E. Minvielle<sup>ae</sup>, G. Mituka<sup>ax</sup>, M. Miura<sup>aw</sup>, K. Mizouchi<sup>az</sup>, J.-P. Mols<sup>h</sup>, L. Monfregola<sup>t</sup>, E. Monmarthe<sup>h</sup>, F. Moreau<sup>n</sup>, B. Morgan<sup>bd</sup>, S. Moriyama<sup>aw</sup>, D. Morris<sup>az</sup>, A. Muir<sup>at</sup>, A. Murakami<sup>ab</sup>, J.F. Muratore<sup>f</sup>, M. Murdoch<sup>ad</sup>, S. Murphy<sup>p</sup>, J. Myslik<sup>ba</sup>, G. Nagashima<sup>ah</sup>, T. Nakadaira<sup>r</sup>, M. Nakahata<sup>aw</sup>, T. Nakamoto<sup>r</sup>, K. Nakamura<sup>r</sup>, S. Nakayama<sup>aw</sup>, T. Nakaya<sup>ab</sup>, D. Naples<sup>al</sup>, B. Nelson<sup>ah</sup>, T.C. Nicholls<sup>au</sup>, K. Nishikawa<sup>r</sup>, H. Nishino<sup>ax</sup>, K. Nitta<sup>ab</sup>, F. Nizery<sup>h</sup>, J.A. Nowak<sup>ae</sup>, M. Noy<sup>u</sup>, Y. Obayashi<sup>aw</sup>, T. Ogitsu<sup>r</sup>, H. Ohhata<sup>r</sup>, T. Okamura<sup>r</sup>, K. Okumura<sup>ax</sup>, T. Okusawa<sup>ai</sup>, C. Ohlmann<sup>az</sup>, K. Olchanski<sup>az</sup>, R. Openshaw<sup>az</sup>, S.M. Oser<sup>e</sup>, M. Otani<sup>ab</sup>, R.A. Owen<sup>am</sup>, Y. Oyama<sup>r</sup>, T. Ozaki<sup>ai</sup>, M.Y. Pac<sup>l</sup>, V. Palladino<sup>w</sup>, V. Paolone<sup>al</sup>, P. Paul<sup>ah</sup>, D. Payne<sup>ad</sup>, G.F. Pearce<sup>au</sup>, C. Pearson<sup>az</sup>, J.D. Perkin<sup>ar</sup>, M. Pflieger<sup>ba</sup>, F. Pierre<sup>l</sup>, D. Pierrepont<sup>h</sup>, P. Plonski<sup>bc</sup>, P. Poffenberger<sup>ba</sup>, E. Poplawska<sup>am</sup>, B. Popov<sup>ak,2</sup>, M. Posiadala<sup>bb</sup>, J.-M. Poutissou<sup>az</sup>, R. Poutissou<sup>az</sup>, R. Preece<sup>au</sup>, P. Przewlocki<sup>b</sup>, W. Qian<sup>au</sup>, J.L. Raaf<sup>d</sup>, E. Radicioni<sup>v</sup>, K. Ramos<sup>ah</sup>, P. Ratoff<sup>ac</sup>, T.M. Rauffer<sup>au</sup>, M. Ravonel<sup>p</sup>, M. Raymond<sup>u</sup>, F. Retiere<sup>az</sup>, D. Richards<sup>bd</sup>, J.-L. Ritou<sup>h</sup>, A. Robert<sup>ak</sup>, P.A. Rodrigues<sup>ao</sup>, E. Rondio<sup>b</sup>, M. Roney<sup>ba</sup>, M. Rooney<sup>au</sup>, D. Ross<sup>az</sup>, B. Rossi<sup>c</sup>, S. Roth<sup>ap</sup>, A. Rubbia<sup>o</sup>, D. Ruterbories<sup>k</sup>, R. Sacco<sup>am</sup>, S. Sadler<sup>ar</sup>, K. Sakashita<sup>r</sup>, F. Sanchez<sup>s</sup>, A. Sarrat<sup>h</sup>, K. Sasaki<sup>r</sup>, P. Schaack<sup>u</sup>, J. Schmidt<sup>ah</sup>, K. Scholberg<sup>m</sup>, J. Schwehr<sup>k</sup>, M. Scott<sup>u</sup>, D.I. Scully<sup>bd</sup>, Y. Seiya<sup>ai</sup>, T. Sekiguchi<sup>r</sup>, H. Sekiya<sup>aw</sup>, G. Sheffer<sup>az</sup>, M. Shibata<sup>r</sup>, Y. Shimizu<sup>ax</sup>, M. Shiozawa<sup>aw</sup>, S. Short<sup>u</sup>, M. Siyad<sup>au</sup>, D. Smith<sup>ae</sup>, R.J. Smith<sup>aj</sup>, M. Smy<sup>g</sup>, J. Sobczyk<sup>bf</sup>, H. Sobel<sup>g</sup>, S. Sooriyakumaran<sup>az</sup>, M. Sorel<sup>t</sup>, J. Spitz<sup>j</sup>, A. Stahl<sup>ap</sup>, P. Stamoulis<sup>t</sup>, O. Star<sup>az</sup>, J. Statter<sup>ac</sup>, L. Stawnczyz<sup>bg</sup>, J. Steinmann<sup>ap</sup>, J. Steffens<sup>ah</sup>, B. Still<sup>am</sup>, M. Stodulski<sup>q</sup>, J. Stone<sup>d</sup>, C. Strabel<sup>o</sup>, T. Strauss<sup>o</sup>, R. Sulej<sup>b,bc</sup>, P. Sutcliffe<sup>ad</sup>, A. Suzuki<sup>aa</sup>, K. Suzuki<sup>ab</sup>, S. Suzuki<sup>r</sup>, S.Y. Suzuki<sup>r</sup>, Y. Suzuki<sup>r</sup>, Y. Suzuki<sup>aw</sup>, J. Swierblewski<sup>q</sup>, T. Szegłowski<sup>as</sup>, M. Szeptycka<sup>b</sup>, R. Tacik<sup>an</sup>, M. Tada<sup>r</sup>, A.S. Tadeballi<sup>ah</sup>, M. Taguchi<sup>ab</sup>, S. Takahashi<sup>ab</sup>, A. Takeda<sup>aw</sup>, Y. Takenaga<sup>aw</sup>, Y. Takeuchi<sup>aa</sup>, H.A. Tanaka<sup>e,3</sup>, K. Tanaka<sup>r</sup>, M. Tanaka<sup>r</sup>, M.M. Tanaka<sup>r</sup>, N. Tanimoto<sup>ax</sup>, K. Tashiro<sup>ai</sup>, I.J. Taylor<sup>ah,u</sup>, A. Terashima<sup>r</sup>, D. Terhorst<sup>ap</sup>, R. Terri<sup>am</sup>, L.F. Thompson<sup>ar</sup>, A. Thorley<sup>ad</sup>, M. Thorpe<sup>au</sup>, W. Toki<sup>k,ah</sup>, T. Tomaru<sup>r</sup>, Y. Totsuka<sup>l</sup>, C. Touramanis<sup>ad</sup>, T. Tsukamoto<sup>r</sup>, V. Tvaskis<sup>ba</sup>, M. Tzanov<sup>ae,j</sup>, Y. Uchida<sup>u</sup>, K. Ueno<sup>aw</sup>, M. Usseglio<sup>h</sup>, A. Vacheret<sup>u</sup>, M. Vagins<sup>g</sup>, J.F. Van Schalkwyk<sup>u</sup>, J.-C. Vanel<sup>n</sup>, G. Vasseur<sup>h</sup>, O. Veledar<sup>ar</sup>, P. Vincent<sup>az</sup>, T. Wachala<sup>q</sup>, A.V. Waldron<sup>aj</sup>, C.W. Walter<sup>m</sup>, P.J. Wanderer<sup>f</sup>, M.A. Ward<sup>ar</sup>, G.P. Ward<sup>ar</sup>, D. Wark<sup>au,u</sup>, D. Warner<sup>k</sup>, M.O. Wascko<sup>u</sup>, A. Weber<sup>aj,au</sup>, R. Wendell<sup>m</sup>, J. Wendland<sup>e</sup>, N. West<sup>aj</sup>, L.H. Whitehead<sup>bd</sup>, G. Wikström<sup>p</sup>, R.J. Wilkes<sup>be</sup>, M.J. Wilking<sup>az</sup>, Z. Williamson<sup>aj</sup>, J.R. Wilson<sup>am</sup>, R.J. Wilson<sup>k</sup>, K. Wong<sup>az</sup>, T. Wongjirad<sup>m</sup>, S. Yamada<sup>aw</sup>, Y. Yamada<sup>r</sup>, A. Yamamoto<sup>r</sup>, K. Yamamoto<sup>ai</sup>, Y. Yamanoi<sup>r</sup>, H. Yamaoka<sup>r</sup>, C. Yanagisawa<sup>ah,4</sup>, T. Yano<sup>aa</sup>, S. Yen<sup>az</sup>, N. Yershov<sup>z</sup>, M. Yokoyama<sup>av</sup>, A. Zalewska<sup>q</sup>, J. Zalipska<sup>e</sup>, K. Zaremba<sup>bc</sup>, M. Ziembicki<sup>bc</sup>, E.D. Zimmerman<sup>j</sup>, M. Zito<sup>h</sup>, J. Zmuda<sup>bf</sup>

<sup>a</sup> University of Alberta, Centre for Particle Physics, Department of Physics, Edmonton, Alberta, Canada

<sup>b</sup> The Andrzej Soltan Institute for Nuclear Studies, Warsaw, Poland

<sup>c</sup> University of Bern, Albert Einstein Center for Fundamental Physics, Laboratory for High Energy Physics (LHEP), Bern, Switzerland

<sup>d</sup> Boston University, Department of Physics, Boston, Massachusetts, USA

<sup>e</sup> University of British Columbia, Department of Physics and Astronomy, Vancouver, British Columbia, Canada

<sup>f</sup> Brookhaven National Laboratory, Physics Department, Upton, New York, USA

<sup>g</sup> University of California, Irvine, Department of Physics and Astronomy, Irvine, California, USA

<sup>h</sup> IRFU, CEA Saclay, Gif-sur-Yvette, France

<sup>i</sup> Chonnam National University, Department of Physics, Kwangju, Korea

<sup>j</sup> University of Colorado at Boulder, Department of Physics, Boulder, Colorado, USA

<sup>k</sup> Colorado State University, Department of Physics, Fort Collins, Colorado, USA

<sup>l</sup> Dongshin University, Department of Physics, Naju, Korea

<sup>m</sup> Duke University, Department of Physics, Durham, North Carolina, USA

<sup>n</sup> Ecole Polytechnique, IN2P3-CNRS, Laboratoire Leprince-Ringuet, Palaiseau, France

<sup>o</sup> ETH Zurich, Institute for Particle Physics, Zurich, Switzerland

<sup>p</sup> University of Geneva, Section de Physique, DPNC, Geneva, Switzerland

<sup>q</sup> H. Niewodniczanski Institute of Nuclear Physics PAN, Cracow, Poland

<sup>r</sup> High Energy Accelerator Research Organization (KEK), Tsukuba, Ibaraki, Japan

<sup>s</sup> Institut de Física d'Altes Energies (IFAE), Bellaterra (Barcelona), Spain

<sup>t</sup> IFIC, CSIC & University of Valencia, Valencia, Spain

<sup>u</sup> Imperial College London, Department of Physics, London, United Kingdom

<sup>v</sup> INFN Sezione di Bari and Università e Politecnico di Bari, Dipartimento Interuniversitario di Fisica, Bari, Italy

<sup>w</sup> INFN Sezione di Napoli and Università di Napoli, Dipartimento di Fisica, Napoli, Italy

<sup>x</sup> INFN Sezione di Padova and Università di Padova, Dipartimento di Fisica, Padova, Italy

<sup>y</sup> INFN Sezione di Roma and Università di Roma "La Sapienza", Roma, Italy

<sup>z</sup> Institute for Nuclear Research of the Russian Academy of Sciences, Moscow, Russia

<sup>aa</sup> Kobe University, Kobe, Japan

<sup>ab</sup> Kyoto University, Department of Physics, Kyoto, Japan

<sup>ac</sup> Lancaster University, Physics Department, Lancaster, United Kingdom

<sup>ad</sup> University of Liverpool, Department of Physics, Liverpool, United Kingdom

<sup>ae</sup> Louisiana State University, Department of Physics and Astronomy, Baton Rouge, Louisiana, USA

<sup>af</sup> Université de Lyon, Université Claude Bernard Lyon 1, IPN Lyon (IN2P3), Villeurbanne, France

- <sup>a8</sup> Miyagi University of Education, Department of Physics, Sendai, Japan  
<sup>a9</sup> State University of New York at Stony Brook, Department of Physics and Astronomy, Stony Brook, New York, USA  
<sup>a1</sup> Osaka City University, Department of Physics, Osaka, Japan  
<sup>a1</sup> Oxford University, Department of Physics, Oxford, United Kingdom  
<sup>a2</sup> UPMC, Université Paris Diderot, CNRS/IN2P3, Laboratoire de Physique Nucléaire et de Hautes Energies (LPNHE), Paris, France  
<sup>a1</sup> University of Pittsburgh, Department of Physics and Astronomy, Pittsburgh, Pennsylvania, USA  
<sup>am</sup> Queen Mary University of London, School of Physics, London, United Kingdom  
<sup>an</sup> University of Regina, Physics Department, Regina, Saskatchewan, Canada  
<sup>a0</sup> University of Rochester, Department of Physics and Astronomy, Rochester, New York, USA  
<sup>ap</sup> RWTH Aachen University, III. Physikalisches Institut, Aachen, Germany  
<sup>a4</sup> Seoul National University, Department of Physics, Seoul, Korea  
<sup>a1</sup> University of Sheffield, Department of Physics and Astronomy, Sheffield, United Kingdom  
<sup>a5</sup> University of Silesia, Institute of Physics, Katowice, Poland  
<sup>a1</sup> STFC, Daresbury Laboratory, Warrington, United Kingdom  
<sup>au</sup> STFC, Rutherford Appleton Laboratory, Harwell Oxford, United Kingdom  
<sup>av</sup> University of Tokyo, Department of Physics, Tokyo, Japan  
<sup>aw</sup> University of Tokyo, Institute for Cosmic Ray Research, Kamioka Observatory, Kamioka, Japan  
<sup>ax</sup> University of Tokyo, Institute for Cosmic Ray Research, Research Center for Cosmic Neutrinos, Kashiwa, Japan  
<sup>ay</sup> University of Toronto, Department of Physics, Toronto, Ontario, Canada  
<sup>az</sup> TRIUMF, Vancouver, British Columbia, Canada  
<sup>ba</sup> University of Victoria, Department of Physics and Astronomy, Victoria, British Columbia, Canada  
<sup>bb</sup> University of Warsaw, Faculty of Physics, Warsaw, Poland  
<sup>bc</sup> Warsaw University of Technology, Institute of Radioelectronics, Warsaw, Poland  
<sup>bd</sup> University of Warwick, Department of Physics, Coventry, United Kingdom  
<sup>be</sup> University of Washington, Department of Physics, Seattle, Washington, USA  
<sup>bf</sup> Wrocław University, Faculty of Physics and Astronomy, Wrocław, Poland  
<sup>bg</sup> York University, Department of Physics and Astronomy, Toronto, Ontario, Canada

## The T2K Collaboration

### ARTICLE INFO

#### Article history:

Received 4 June 2011

Received in revised form

5 June 2011

Accepted 5 June 2011

Available online 30 June 2011

#### Keywords:

Neutrinos

Neutrino oscillation

Long baseline

T2K

J-PARC

Super-Kamiokande

### ABSTRACT

The T2K experiment is a long baseline neutrino oscillation experiment. Its main goal is to measure the last unknown lepton sector mixing angle  $\theta_{13}$  by observing  $\nu_e$  appearance in a  $\nu_\mu$  beam. It also aims to make a precision measurement of the known oscillation parameters,  $\Delta m_{23}^2$  and  $\sin^2 2\theta_{23}$ , via  $\nu_\mu$  disappearance studies. Other goals of the experiment include various neutrino cross-section measurements and sterile neutrino searches. The experiment uses an intense proton beam generated by the J-PARC accelerator in Tokai, Japan, and is composed of a neutrino beamline, a near detector complex (ND280), and a far detector (Super-Kamiokande) located 295 km away from J-PARC. This paper provides a comprehensive review of the instrumentation aspect of the T2K experiment and a summary of the vital information for each subsystem.

© 2011 Elsevier B.V. Open access under [CC BY-NC-ND license](#).

## 1. Introduction

The T2K (Tokai-to-Kamioka) experiment [1] is a long baseline neutrino oscillation experiment designed to probe the mixing of the muon neutrino with other species and shed light on the neutrino mass scale. It is the first long baseline neutrino oscillation experiment proposed and approved to look explicitly for the electron neutrino appearance from the muon neutrino, thereby measuring  $\theta_{13}$ , the last unknown mixing angle in the lepton sector.

T2K's physics goals include the measurement of the neutrino oscillation parameters with precision of  $\delta(\Delta m_{23}^2) \sim 10^{-4} \text{ eV}^2$  and  $\delta(\sin^2 2\theta_{23}) \sim 0.01$  via  $\nu_\mu$  disappearance studies, and achieving a factor of about 20 better sensitivity compared to the current best

limit on  $\theta_{13}$  from the CHOOZ experiment [2] through the search for  $\nu_\mu \rightarrow \nu_e$  appearance ( $\sin^2 2\theta_{\mu e} \simeq \frac{1}{2} \sin^2 2\theta_{13} > 0.004$  at 90% CL for CP violating phase  $\delta = 0$ ). In addition to neutrino oscillation studies, the T2K neutrino beam (with  $E_\nu \sim 1 \text{ GeV}$ ) will enable a rich fixed-target physics program of neutrino interaction studies at energies covering the transition between the resonance production and deep inelastic scattering regimes.

T2K uses Super-Kamiokande [3] as the far detector to measure neutrino rates at a distance of 295 km from the accelerator, and near detectors to sample the beam just after production. The experiment includes a neutrino beamline and a near detector complex at 280 m (ND280), both of which were newly constructed. Super-Kamiokande was upgraded and restored to 40% photocathode coverage (the same as the original Super-Kamiokande detector) with new photomultiplier tubes in 2005–06, following the accident of 2001. Fig. 1 shows a schematic layout of the T2K experiment as a whole.

T2K adopts the off-axis method [4] to generate the narrow-band neutrino beam using the new MW-class proton synchrotron

<sup>1</sup> Deceased.

<sup>2</sup> Also at JINR, Dubna, Russia.

<sup>3</sup> Also at Institute of Particle Physics, Canada.

<sup>4</sup> Also at BMCC/CUNY, New York, New York, USA.

\* Corresponding author.

E-mail address: chang.jung@stonybrook.edu (C.K. Jung).

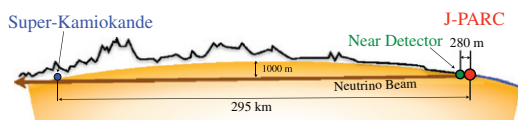


**Fig. 1.** A schematic of a neutrino's journey from the neutrino beamline at J-PARC, through the near detectors (green dot) which are used to determine the properties of the neutrino beam, and then 295 km underneath the main island of Japan to Super-Kamiokande. (For interpretation of the references to color in this figure legend, the reader is referred to the web version of this article.)

at J-PARC<sup>5</sup>. In this method the neutrino beam is purposely directed at an angle with respect to the baseline connecting the proton target and the far detector, Super-Kamiokande. The off-axis angle is set at  $2.5^\circ$  so that the narrow-band muon neutrino beam generated toward the far detector has a peak energy at  $\sim 0.6$  GeV, which maximizes the effect of the neutrino oscillation at 295 km and minimizes the background to electron neutrino appearance detection. The angle can be reduced to  $2.0^\circ$ , allowing variation of the peak neutrino energy, if necessary.

The near detector site at  $\sim 280$  m from the production target houses on-axis and off-axis detectors. The on-axis detector (INGRID), composed of an array of iron/scintillator sandwiches, measures the neutrino beam direction and profile. The off-axis detector, immersed in a magnetic field, measures the muon neutrino flux and energy spectrum, and intrinsic electron neutrino contamination in the beam in the direction of the far detector, along with measuring rates for exclusive neutrino reactions. These measurements are essential in order to characterize signals and backgrounds that are observed in the Super-Kamiokande far detector.

The off-axis detector is composed of: a water-scintillator detector optimized to identify  $\pi^0$ 's (the PØD); the tracker consisting of time projection chambers (TPCs) and fine grained detectors (FGDs) optimized to study charged current interactions; and an electromagnetic calorimeter (ECal) that surrounds the (PØD) and the tracker. The whole off-axis detector is placed in a 0.2 T magnetic field provided by the recycled UA1 magnet, which also serves as part of a side muon range detector (SMRD).

The far detector, Super-Kamiokande, is located in the Mozumi mine of the Kamioka Mining and Smelting Company, near the village of Higashi-Mozumi, Gifu, Japan. The detector cavity lies under the peak of Mt. Ikenoyama, with 1000 m of rock, or 2700 m-water-equivalent (m.w.e.) mean overburden. It is a water Cherenkov detector consisting of a welded stainless steel tank, 39 m in diameter and 42 m tall, with a total nominal water capacity of 50,000 tons. The detector contains approximately 13,000 photomultiplier tubes (PMTs) that image neutrino interactions in pure water. Super-Kamiokande has been running since 1996 and has had four distinctive running periods. The latest period, SK-IV, is running stably and features upgraded PMT readout electronics. A detailed description of the detector can be found elsewhere [3].

Construction of the neutrino beamline started in April 2004. The complete chain of accelerator and neutrino beamline was successfully commissioned during 2009, and T2K began accumulating neutrino beam data for physics analysis in January 2010.

Construction of the majority of the ND280 detectors was completed in 2009 with the full installation of INGRID, the central ND280 off-axis sub detectors (PØD, FGD, TPC and downstream ECal) and the SMRD. The ND280 detectors began stable operation in

**Table 1**  
Machine design parameters of the J-PARC MR for the fast extraction.

Circumference	1567 m
Beam power	$\sim 750$ kW
Beam kinetic energy	30 GeV
Beam intensity	$\sim 3 \times 10^{14}$ p/spill
Spill cycle	$\sim 0.5$ Hz
Number of bunches	8/spill
RF frequency	1.67–1.72 MHz
Spill width	$\sim 5$ $\mu$ s

February 2010. The rest of the ND280 detector (the ECals) was completed in the fall of 2010.

The T2K collaboration consists of over 500 physicists and technical staff members from 59 institutions in 12 countries (Canada, France, Germany, Italy, Japan, Poland, Russia, South Korea, Spain, Switzerland, the United Kingdom and the United States).

This paper provides a comprehensive review of the instrumentation aspect of the T2K experiment and a summary of the vital information for each subsystem. Detailed descriptions of some of the major subsystems, and their performance, will be presented in separate technical papers.

## 2. J-PARC accelerator

J-PARC, which was newly constructed at Tokai, Ibaraki, consists of three accelerators [5]: a linear accelerator (LINAC), a rapid-cycling synchrotron (RCS) and the main ring (MR) synchrotron. An  $H^-$  beam is accelerated up to 400 MeV<sup>6</sup> (181 MeV at present) by the LINAC, and is converted to an  $H^+$  beam by charge-stripping foils at the RCS injection. The beam is accelerated up to 3 GeV by the RCS with a 25 Hz cycle. The harmonic number of the RCS is two, and there are two bunches in a cycle. About 5% of these bunches are supplied to the MR. The rest of the bunches are supplied to the muon and neutron beamline in the Material and Life Science Facility. The proton beam injected into the MR is accelerated up to 30 GeV. The harmonic number of the MR is nine, and the number of bunches in the MR is eight (six before June 2010). There are two extraction points in the MR: slow extraction for the hadron beamline and fast extraction for the neutrino beamline.

In the fast extraction mode, the eight circulating proton bunches are extracted within a single turn by a set of five kicker magnets. The time structure of the extracted proton beam is key to discriminating various backgrounds, including cosmic rays, in the various neutrino detectors. The parameters of the J-PARC MR for the fast extraction are listed in Table 1.

## 3. T2K neutrino beamline

Each proton beam spill consists of eight proton bunches extracted from the MR to the T2K neutrino beamline, which produces the neutrino beam.

The neutrino beamline is composed of two sequential sections: the primary and secondary beamlines. In the primary beamline, the extracted proton beam is transported to point toward Kamioka. In the secondary beamline, the proton beam impinges on a target to produce secondary pions, which are focused by magnetic horns and decay into neutrinos. An overview of the neutrino beamline is shown in Fig. 2. Each component of the beamline is described in this section.

<sup>5</sup> Japan Proton Accelerator Research Complex jointly constructed and operated by KEK and JAEA.

<sup>6</sup> Note that from here on all accelerator beam energy given are kinetic energies.

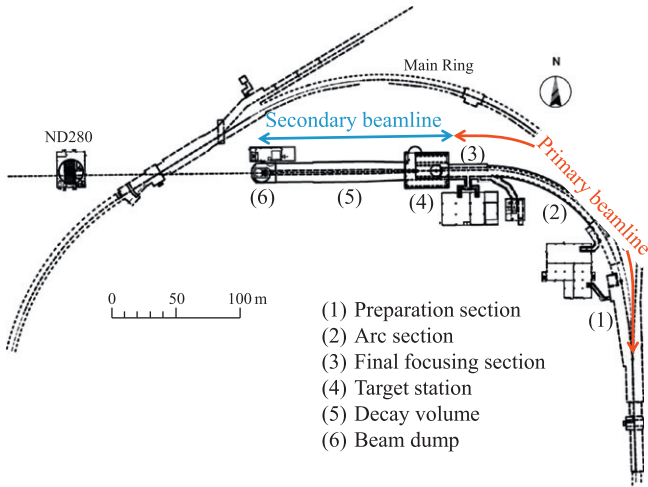


Fig. 2. Overview of the T2K neutrino beamline.

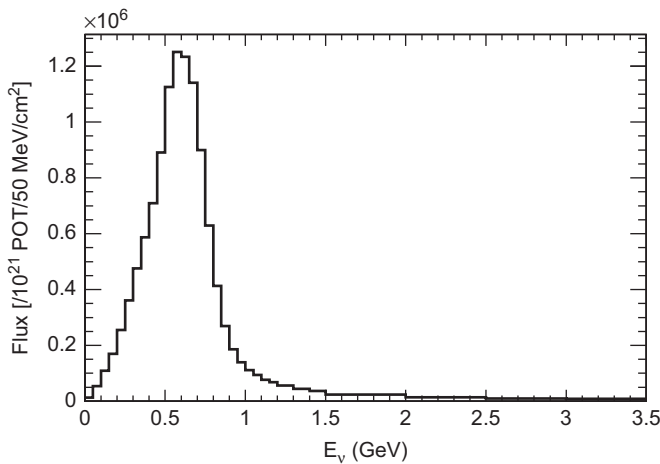


Fig. 3. The unoscillated  $\nu_\mu$  flux at Super-Kamiokande with an off-axis angle of  $2.5^\circ$  when the electromagnetic horns are operated at 250 kA.

The neutrino beamline is designed so that the neutrino energy spectrum at Super-Kamiokande can be tuned by changing the off-axis angle down to a minimum of  $\sim 2.0^\circ$ , from the current (maximum) angle of  $\sim 2.5^\circ$ . The unoscillated  $\nu_\mu$  flux at Super-Kamiokande with this off-axis angle is shown in Fig. 3. Precise measurements of the baseline distance and off-axis angle were determined by a GPS survey, described in Section 3.6.1.

### 3.1. Primary beamline

The primary beamline consists of the preparation section (54 m long), arc section (147 m) and final focusing section (37 m). In the preparation section, the extracted proton beam is tuned with a series of 11 normal conducting magnets (four steering, two dipole and five quadrupole magnets) so that the beam can be accepted by the arc section. In the arc section, the beam is bent toward the direction of Kamioka by  $80.7^\circ$ , with a 104 m radius of curvature, using 14 doublets of superconducting combined function magnets (SCFMs) [6–8]. There are also three pairs of horizontal and vertical superconducting steering magnets to correct the beam orbit. In the final focusing section, 10 normal conducting magnets (four steering, two dipole and four quadrupole magnets) guide and focus the beam onto the target, while directing the beam downward by  $3.637^\circ$  with respect to the horizontal.

A well-tuned proton beam is essential for stable neutrino beam production, and to minimize beam loss in order to achieve high-power beam operation. Therefore, the intensity, position, profile and loss of the proton beam in the primary sections are precisely monitored by five current transformers (CTs), 21 electrostatic monitors (ESMs), 19 segmented secondary emission monitors (SSEMs) and 50 beam loss monitors (BLMs), respectively. Photographs of the monitors are shown in Fig. 4, while the monitor locations are shown in Fig. 5. Polyimide cables and ceramic feedthroughs are used for the beam monitors, because of their radiation tolerance.

The beam pipe is kept at  $\sim 3 \times 10^{-6}$  Pa using ion pumps, in order to be connected with the beam pipe of the MR and to reduce the heat load to the SCFMs. The downstream end of the beam pipe is connected to the “monitor stack”: the 5 m tall vacuum vessel embedded within the 70 cm thick wall between the primary beamline and secondary beamline. The most downstream ESM and SSEM are installed in the monitor stack. Because of the high residual radiation levels, the monitor stack is equipped with a remote-handling system for the monitors.

#### 3.1.1. Normal conducting magnet

The normal conducting magnets are designed to be tolerant of radiation and to be easy to maintain in the high-radiation environment. For the four most upstream magnets in the preparation



Fig. 4. Photographs of the primary beamline monitors. Upper left: CT. Upper right: ESM. Lower left: SSEM. Lower right: BLM.

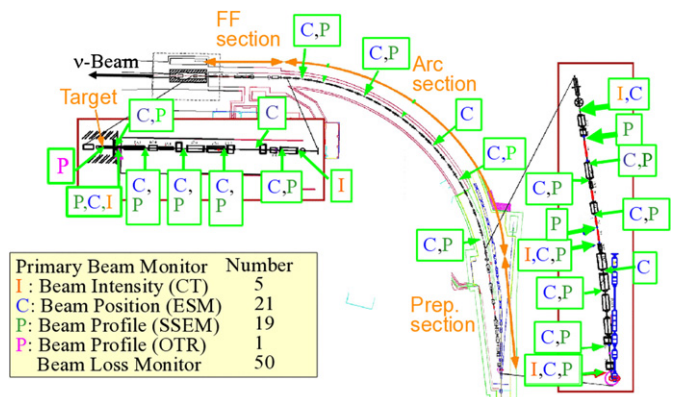


Fig. 5. Location of the primary beamline monitors.

section, a mineral insulation coil is used because of its radiation tolerance. To minimize workers' exposure to radiation, remote maintenance systems are installed such as twistlock slings, alignment dowel pins, and quick connectors for cooling pipes and power lines.

For the quadrupole magnets, "flower-shaped" beam pipes, whose surfaces were made in the shape of the magnetic pole surface, are adopted to maximize their apertures.

### 3.1.2. Superconducting combined function magnet (SCFM)

In total, there are 28 SCFMs [9–12], each with a coil aperture of 173.4 mm. The operating current for a 30 GeV proton beam is 4360 A, while the magnets themselves were tested up to 7500 A, which corresponds to a 50 GeV proton beam.

The combined field is generated with a left–right asymmetric single layer Rutherford-type coil, made of NbTi/Cu. Two SCFMs are enclosed in one cryostat in forward and backward directions to constitute a defocus–focus doublet, while each dipole field is kept in the same direction. All the SCFMs are cooled in series with supercritical helium at 4.5 K and are excited with a power supply (8 kA, 10 V).

There are also three superconducting corrector dipole magnets, which are cooled by conduction, in the SCFM section. Each magnet has two windings, one for vertical and one for horizontal deflections. These magnets allow the beam to be precisely positioned along the beamline (to minimize losses).

The magnet safety system (MSS) protects the magnets and the bus-bars of the primary beamline in the case of an abnormal condition, and supplements the passive safety protection provided by cold diodes mounted in parallel with the superconducting magnets. The MSS is based on the detection of a resistive voltage difference across the magnet that would appear in the case of a quench. It then secures the system by shutting down the magnet power supply and issuing a beam abort interlock signal. Most units of the MSS are dual redundant. This redundancy increases the reliability of the system. The MSS is based on 33 MD200 boards [13].

### 3.1.3. Beam intensity monitor

Beam intensity is measured with five current transformers (CTs). Each CT is a 50-turn toroidal coil around a cylindrical ferromagnetic core. To achieve high-frequency response up to 50 MHz for the short-pulsed bunches and to avoid saturation caused by a large peak current of 200 A, CTs use a FINEMET<sup>®</sup> (nanocrystalline Fe-based soft magnetic material) core, which has a high saturation flux density, high relative permeability and low core loss over a wide frequency range. The core's inner diameter is 260 mm, its outer diameter is 340 mm and it has a mass of 7 kg. It is impregnated with epoxy resin. To achieve high radiation hardness, polyimide tape and alumina fiber tape are used to insulate the core and wire. Each CT is covered by an iron shield to block electromagnetic noise.

Each CT's signal is transferred through about 100 m of 20D colgate cable and read by a 160 MHz Flash ADC (FADC). The CT is calibrated using another coil around the core, to which a pulse current, shaped to emulate the passage of a beam bunch, is applied. The CT measures the absolute proton beam intensity with a 2% uncertainty and the relative intensity with a 0.5% fluctuation. It also measures the beam timing with precision better than 10 ns.

### 3.1.4. Beam position monitor

Each electrostatic monitor (ESM) has four segmented cylindrical electrodes surrounding the proton beam orbit (80° coverage per electrode). By measuring top–bottom and left–right asymmetry of the beam-induced current on the electrodes, it monitors the

proton beam center position nondestructively (without direct interaction with the beam).

The longitudinal length of an ESM is 125 mm for the 15 ESMs in the preparation and final focusing sections, 210 mm for the five ESMs in the arc section and 160 mm for the ESM in the monitor stack. The signal from each ESM is read by a 160 MHz FADC.

The measurement precision of the beam position is less than 450  $\mu\text{m}$  (20–40  $\mu\text{m}$  for the measurement fluctuation, 100–400  $\mu\text{m}$  for the alignment precision and 200  $\mu\text{m}$  for the systematic uncertainty other than the alignment), while the requirement is 500  $\mu\text{m}$ .

### 3.1.5. Beam profile monitor

Each segmented secondary emission monitor (SSEM) has two thin (5  $\mu\text{m}$ ,  $10^{-5}$  interaction lengths) titanium foils stripped horizontally and vertically, and an anode HV foil between them. The strips are hit by the proton beam and emit secondary electrons in proportion to the number of protons that go through the strip. The electrons drift along the electric field and induce currents on the strips. The induced signals are transmitted to 65 MHz FADCs through twisted-pair cables. The proton beam profile is reconstructed from the corrected charge distribution on a bunch-by-bunch basis. The strip width of each SSEM ranges from 2 to 5 mm, optimized according to the expected beam size at the installed position. The systematic uncertainty of the beam width measurement is 200  $\mu\text{m}$  while the requirement is 700  $\mu\text{m}$ . Optics parameters of the proton beam (Twiss parameters and emittance) are reconstructed from the profiles measured by the SSEMs, and are used to estimate the profile center, width and divergence at the target.

Since each SSEM causes beam loss (0.005% loss), they are remotely inserted into the beam orbit only during beam tuning, and extracted from the beam orbit during continuous beam operation.

### 3.1.6. Beam loss monitor

To monitor the beam loss, 19 and 10 BLMs are installed near the beam pipe in the preparation and final focusing sections, respectively, while 21 BLMs are positioned near the SCFMs in the arc section. Each BLM (Toshiba Electron Tubes & Devices E6876-400) is a wire proportional counter filled with an Ar–CO<sub>2</sub> mixture [14].

The signal is integrated during the spill and if it exceeds a threshold, a beam abort interlock signal is fired. The raw signal before integration is read by the FADCs with 30 MHz sampling for the software monitoring.

By comparing the beam loss with and without the SSEMs in the beamline, it was shown that the BLM has a sensitivity down to a 16 mW beam loss. In the commissioning run, it was confirmed that the residual dose and BLM data integrated during the period have good proportionality. This means that the residual dose can be monitored by watching the BLM data.

## 3.2. Secondary beamline

Produced pions decay in flight inside a single volume of  $\sim 1500\text{ m}^3$ , filled with helium gas (1 atm) to reduce pion absorption and to suppress tritium and NO<sub>x</sub> production by the beam. The helium vessel is connected to the monitor stack via a titanium-alloy beam window which separates the vacuum in the primary beamline and the helium gas volume in the secondary beamline. Protons from the primary beamline are directed to the target via the beam window.

The secondary beamline consists of three sections: the target station, decay volume and beam dump (Fig. 6). The target station contains: a baffle which is a collimator to protect the magnetic horns; an optical transition radiation monitor (OTR) to monitor the proton beam profile just upstream of the target; the target to generate secondary pions; and three magnetic horns excited by

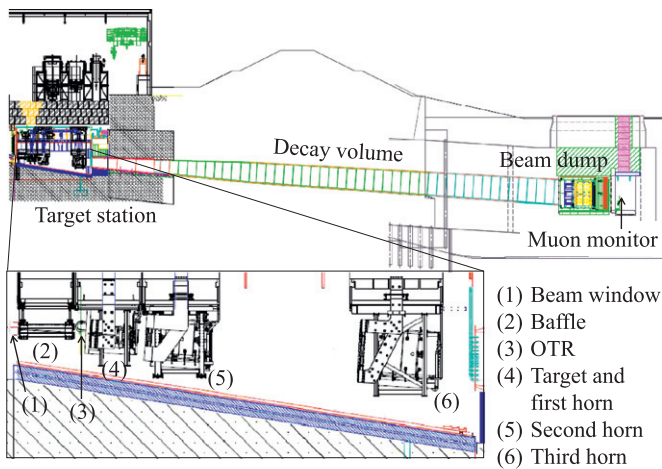


**Fig. 6.** Side view of the secondary beamline. The length of the decay volume is  $\sim 96$  m.

a 250 kA (designed for up to 320 kA) current pulse to focus the pions. The produced pions enter the decay volume and decay mainly into muons and muon neutrinos. All the hadrons, as well as muons below  $\sim 5$  GeV/c, are stopped by the beam dump. The neutrinos pass through the beam dump and are used for physics experiments. Any muons above  $\sim 5$  GeV/c that also pass through the beam dump are monitored to characterize the neutrino beam.

### 3.2.1. Target station

The target station consists of the baffle, OTR, target, and horns, all located inside a helium vessel. The target station is separated from the primary beamline by a beam window at the upstream end, and is connected to the decay volume at the downstream end.

The helium vessel, which is made of 10 cm thick steel, is 15 m long, 4 m wide and 11 m high. It is evacuated down to 50 Pa before it is filled with helium gas. Water cooling channels, called plate coils, are welded to the surface of the vessel, and  $\sim 30^\circ\text{C}$  water cools the vessel to prevent its thermal deformation. An iron shield with a thickness of  $\sim 2$  m and a concrete shield with a thickness of  $\sim 1$  m are installed above the horns inside the helium vessel. Additionally,  $\sim 4.5$  m thick concrete shields are installed above the helium vessel.

The equipment and shields inside the vessel are removable by remote control in case of maintenance or replacement of the horns or target. Beside the helium vessel, there is a maintenance area where manipulators and a lead-glass window are installed, as well as a depository for radio-activated equipment.

### 3.2.2. Beam window

The beam window, comprising two helium-cooled 0.3 mm thick titanium-alloy skins, separates the primary proton beamline vacuum from the target station. The beam window assembly is sealed both upstream and downstream by inflatable bellows vacuum seals to enable it to be removed and replaced if necessary.

### 3.2.3. Baffle

The baffle is located between the beam window and OTR. It is a 1.7 m long, 0.3 m wide and 0.4 m high graphite block, with a beam hole of 30 mm in diameter. The primary proton beam goes through this hole. It is cooled by water cooling pipes.

### 3.2.4. Optical transition radiation monitor

The OTR has a thin titanium-alloy foil, which is placed at  $45^\circ$  to the incident proton beam. As the beam enters and exits the foil,

visible light (transition radiation) is produced in a narrow cone around the beam. The light produced at the entrance transition is reflected at  $90^\circ$  to the beam and directed away from the target area. It is transported in a dogleg path through the iron and concrete shielding by four aluminum  $90^\circ$  off-axis parabolic mirrors to an area with lower radiation levels. It is then collected by a charge injection device camera to produce an image of the proton beam profile.

The OTR has an eight-position carousel holding four titanium-alloy foils, an aluminum foil, a fluorescent ceramic foil of  $100\ \mu\text{m}$  thickness, a calibration foil and an empty slot (Fig. 7). A stepping motor is used to rotate the carousel from one foil to the next. The aluminum (higher reflectivity than titanium) and ceramic (which produces fluorescent light with higher intensity than OTR light) foils are used for low and very low intensity beam, respectively. The calibration foil has precisely machined fiducial holes, of which an image can be taken using back-lighting from lasers and filament lights. It is used for monitoring the alignment of the OTR system. The empty slot allows back-lighting of the mirror system to study its transport efficiency.

### 3.2.5. Target

The target core is a 1.9 interaction length (91.4 cm long), 2.6 cm diameter and  $1.8\ \text{g}/\text{cm}^3$  graphite rod. If a material significantly denser than graphite were used for the target core, it would be melted by the pulsed beam heat load.

The core and a surrounding 2 mm thick graphite tube are sealed inside a titanium case which is 0.3 mm thick. The target assembly is supported as a cantilever inside the bore of the first horn inner conductor with a positional accuracy of 0.1 mm. The target is cooled by helium gas flowing through the gaps between the core and tube and between the tube and case. For the 750 kW

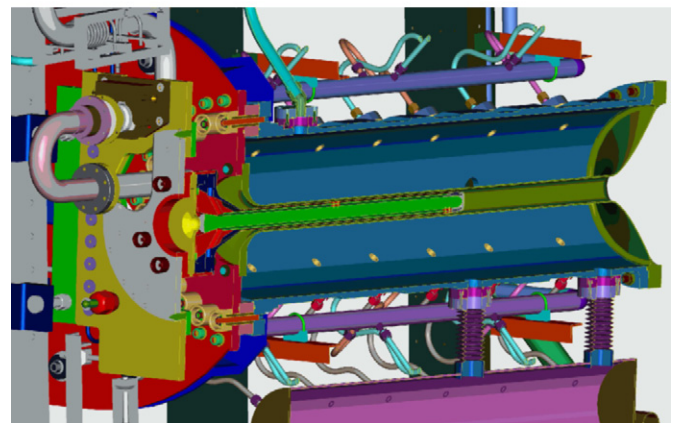
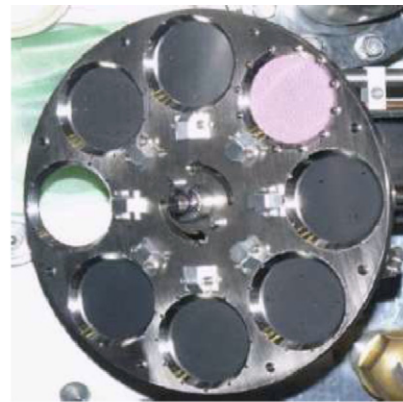


**Fig. 7.** Top: Photograph of the OTR carousel. Bottom: Cross section of the first horn and target.

beam, the flow rate is  $\sim 32$  g/s helium gas with a helium outlet pressure of 0.2 MPa, which corresponds to a flow speed of  $\sim 250$  m/s. When the 750 kW proton beam interacts with the target, the temperature at the center is expected to reach 700 °C, using the conservative assumption that radiation damage has reduced the thermal conductivity of the material by a factor of four.

The radiation dose due to the activation of the target is estimated at a few Sv/h six months after a one year's irradiation by the 750 kW beam [15].

### 3.2.6. Magnetic horn

The T2K beamline uses three horns. Each magnetic horn consists of two coaxial (inner and outer) conductors which encompass a closed volume [16,17]. A toroidal magnetic field is generated in that volume. The field varies as  $1/r$ , where  $r$  is the distance from the horn axis. The first horn collects the pions which are generated at the target installed in its inner conductor. The second and third horns focus the pions. When the horn is run with a operation current of 320 kA, the maximum field is 2.1 T and the neutrino flux at Super-Kamiokande is increased by a factor of  $\sim 16$  (compared to horns at 0 kA) at the spectrum peak energy ( $\sim 0.6$  GeV).

The horn conductor is made of aluminum alloy (6061-T6). The horns' dimensions (minimum inside diameter, inner conductor thickness, outside diameter and length, respectively) are 54 mm, 3 mm, 400 mm and 1.5 m for the first horn, 80 mm, 3 mm, 1000 mm and 2 m for the second horn, and 140 mm, 3 mm, 1400 mm and 2.5 m for the third horn. They are optimized to maximize the neutrino flux; the inside diameter is as small as possible to achieve the maximum magnetic field, and the conductor is as thin as possible to minimize pion absorption while still being tolerant of the Lorentz force, created from the 320 kA current and the magnetic field, and the thermal shock from the beam.

The pulse current is applied via a pulse transformer with a turn ratio of 10:1, which is installed beside the helium vessel in the target station. The horns are connected to the secondary side of the pulse transformer in series using aluminum bus-bars. The currents on the bus-bars are monitored by four Rogowski coils per horn with a 200 kHz FADC readout. The measurement uncertainty of the absolute current is less than  $\sim 2\%$ . The horn magnetic field was measured with a Hall probe before installation, and the uncertainty of the magnetic field strength is approximately 2% for the first horn and less than 1% for the second and third horns.

### 3.2.7. Decay volume

The decay volume is a  $\sim 96$  m long steel tunnel. The cross section is 1.4 m wide and 1.7 m high at the upstream end, and 3.0 m wide and 5.0 m high at the downstream end. The decay volume is surrounded by 6 m thick reinforced concrete shielding. Along the beam axis, 40 plate coils are welded on the steel wall, whose thickness is 16 mm, to cool the wall and concrete to below 100 °C using water.

### 3.2.8. Beam dump

The beam dump sits at the end of the decay volume. The distance between the center of the target and the upstream surface of the beam dump along the neutrino beam direction for the off-axis angle of  $2.5^\circ$  is 109 m. The beam dump's core is made of 75 tons of graphite ( $1.7$  g/cm<sup>3</sup>), and is 3.174 m long, 1.94 m wide and 4.69 m high. It is contained in the helium vessel. Fifteen iron plates are placed outside the vessel and two inside, at the downstream end of the graphite core, to give a total iron

thickness of 2.40 m. Only muons above  $\sim 5.0$  GeV/c can go through the beam dump to reach the downstream muon pit.

The core is sandwiched on both sides by aluminum cooling modules which contain water channels. The temperature in the center of the core is kept at around 150 °C for the 750 kW beam.

## 3.3. Muon monitor

The neutrino beam intensity and direction can be monitored on a bunch-by-bunch basis by measuring the distribution profile of muons, because muons are mainly produced along with neutrinos from the pion two-body decay. The neutrino beam direction is determined to be the direction from the target to the center of the muon profile. The muon monitor [18,19] is located just behind the beam dump. The muon monitor is designed to measure the neutrino beam direction with a precision better than 0.25 mrad, which corresponds to a 3 cm precision of the muon profile center. It is also required to monitor the stability of the neutrino beam intensity with a precision better than 3%.

A detector made of nuclear emulsion was installed just downstream of the muon monitor to measure the absolute flux and momentum distribution of muons.

### 3.3.1. Characteristics of the muon flux

Based on the beamline simulation package, described in Section 3.5, the intensity of the muon flux at the muon monitor, for  $3.3 \times 10^{14}$  protons/spill and 320 kA horn current, is estimated to be  $1 \times 10^7$  charged particles/cm<sup>2</sup>/bunch with a Gaussian-like profile around the beam center and approximately 1 m in width. The flux is composed of around 87% muons, with delta-rays making up the remainder.

### 3.3.2. Muon monitor detectors

The muon monitor consists of two types of detector arrays: ionization chambers at 117.5 m from the target and silicon PIN photodiodes at 118.7 m (Fig. 8). Each array holds 49 sensors at  $25$  cm  $\times$   $25$  cm intervals and covers a  $150 \times 150$  cm<sup>2</sup> area. The collected charge on each sensor is read out by a 65 MHz FADC. The 2D muon profile is reconstructed in each array from the distribution of the observed charge.

The arrays are fixed on a support enclosure for thermal insulation. The temperature inside the enclosure is kept at around 34 °C (within  $\pm 0.7$  °C variation) with a sheathed heater, as the

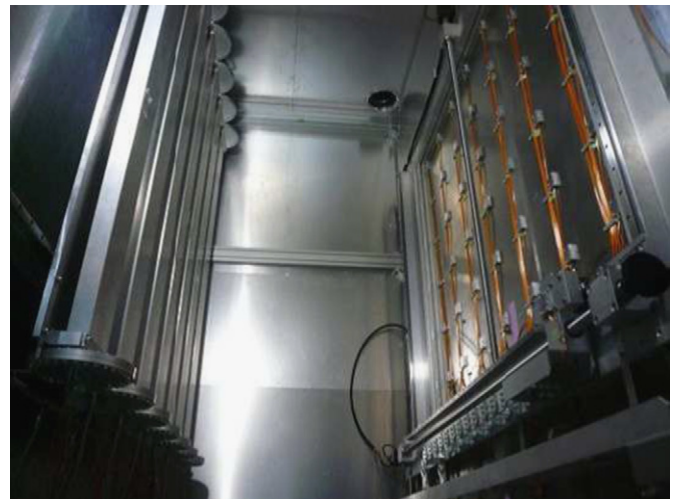


Fig. 8. Photograph of the muon monitor inside the support enclosure. The silicon PIN photodiode array is on the right side and the ionization chamber array is on the left side. The muon beam enters from the left side.

signal gain in the ionization chamber is dependent on the gas temperature.

An absorbed dose at the muon monitor is estimated to be about 100 kGy for a 100-day operation at 750 kW. Therefore, every component in the muon pit is made of radiation-tolerant and low-activation material such as polyimide, ceramic, or aluminum.

### 3.3.3. Ionization chamber

There are seven ionization chambers, each of which contains seven sensors in a  $150 \times 50 \times 1956 \text{ mm}^3$  aluminum gas tube. The  $75 \times 75 \times 3 \text{ mm}^3$  active volume of each sensor is made by two parallel plate electrodes on alumina-ceramic plates. Between the electrodes, 200 V is applied.

Two kinds of gas are used for the ionization chambers according to the beam intensity: Ar with 2% N<sub>2</sub> for low intensity, and He with 1% N<sub>2</sub> for high-intensity. The gas is fed in at approximately 100 cm<sup>3</sup>/min. The gas temperature, pressure and oxygen contamination are kept at around 34 °C with a 1.5 °C gradient and  $\pm 0.2 \text{ °C}$  variation, at  $130 \pm 0.2 \text{ kPa}$  (absolute), and below 2 ppm, respectively.

### 3.3.4. Silicon PIN photodiode

Each silicon PIN photodiode (Hamamatsu ® S3590-08) has an active area of  $10 \times 10 \text{ mm}^2$  and a depletion layer thickness of 300  $\mu\text{m}$ . To fully deplete the silicon layer, 80 V is applied.

The intrinsic resolution of the muon monitor is less than 0.1% for the intensity and less than 0.3 cm for the profile center.

### 3.3.5. Emulsion tracker

The emulsion trackers are composed of two types of modules. The module for the flux measurement consists of eight consecutive emulsion films [20]. It measures the muon flux with a systematic uncertainty of 2%. The other module for the momentum measurement is made of 25 emulsion films interleaved by 1 mm lead plates, which can measure the momentum of each particle by multiple Coulomb scattering with a precision of 28% at a muon energy of 2 GeV/c [21,22]. These films are analyzed by scanning microscopes [23,24].

## 3.4. Beamline online system

For the stable and safe operation of the beamline, the online system collects information on the beamline equipment and the beam measured by the beam monitors, and feeds it back to the operators. It also provides Super-Kamiokande with the spill information for event synchronization by means of GPS, which is described in detail in Section 3.6.2.

### 3.4.1. DAQ system

The signals from each beam monitor are brought to one of five front-end stations in different buildings beside the beamline. The SSEM, BLM, and horn current signals are digitized by a 65 MHz FADC in the COPPER system [25]. The CT and ESM signals are digitized by a 160 MHz VME FADC [26]. The GPS for the event synchronization and the OTR both use custom-made readout electronics. All of these readout systems are managed by the MIDAS framework [27], and the event builder records fully concatenated events every spill, before the next spill is issued. MIDAS's event monitoring system locks the internal data holding buffer. To minimize the locking time, which can have a negative effect on the DAQ system's response time, an event distributor was developed. It receives event data from the MIDAS server and distributes the data in ROOT format to the clients. No reduction is

applied to the output from the ADCs and the event data size remains constant at 1.6 MB.

### 3.4.2. Beamline control system

Information on the beamline (the beam monitor outputs, spill number and status of the beamline equipment) is recorded by EPICS [28]. EPICS also controls the beamline equipment using programmable logic controllers (PLCs).

Based on the data from EPICS, the beam orbit and optics are simulated by SAD [29], and the magnet currents to be adjusted are also calculated.

### 3.4.3. Interlock

The function of the interlock system is to protect people (PPS: person protection system) and the machines (MPS: machine protection system). The PPS can be fired by an emergency stop button, or safety sensors such as door interlocks and radiation monitors. The MPS can be fired by a quenching of the SCFMs, an error from the normal conducting magnet or horn system, an excess in the loss monitor signal, or other machine-related causes.

## 3.5. Beamline simulation for neutrino flux estimation

The neutrino flux is predicted by a Monte Carlo simulation based on experimental data. Specifically, hadron production by 30 GeV protons on a graphite target was measured by a dedicated experiment, NA61/SHINE [30,31], which fully covers the kinematic region of interest for T2K.

In the beam MC, the detailed geometry of the secondary beamline is described in the code. Protons with a kinetic energy of 30 GeV are injected into the graphite target and then secondary particles are produced and focused in the horn magnets. The secondaries and any un-interacted protons are tracked until they decay into neutrinos or are stopped at the beam dump. The tracks of neutrinos are extrapolated to the near and far detectors, providing the predicted fluxes and energy spectra at both detector sites.

The primary interaction of the 30 GeV proton with carbon is simulated based on NA61/SHINE data. Other hadronic interactions inside the target are simulated by FLUKA [32]. The interactions outside the target are simulated using GEANT3/GCALOR [33] with the interaction cross sections tuned to experimental data.

## 3.6. Global alignment and time synchronization

### 3.6.1. Global position survey and alignment

In a long baseline neutrino experiment, controlling the direction of the neutrino beam is one of the most important aspects. For the T2K neutrino experiment, it is necessary to consider the three-dimensional geometry of the earth, since it covers a distance of  $\sim 300 \text{ km}$  from J-PARC to Super-Kamiokande. Determining the correct direction is not simple. Therefore, surveys were performed, including a long baseline GPS survey between Tokai and Kamioka.

Based on the surveys, the primary beamline components, target, and horns were aligned in order to send the neutrino beam in the right direction. The muon monitor and the neutrino near detectors were also aligned in order to monitor the neutrino beam direction. A good alignment of the components is also necessary in order to reduce irradiation in a high-intensity proton beamline.

A complete neutrino beamline survey is carried out on a yearly basis. There are five penetration holes in the neutrino beamline to connect a ground survey network with an underground survey; one at the preparation section, two at the final focusing section and two at the muon pit. In the target station, the underground survey points were transferred to the ground level so that they

can be monitored even after the underground helium vessel is closed. In the primary beamline, a survey and alignment is carried out using a laser tracker with a spatial resolution of  $50\ \mu\text{m}$  at a distance shorter than 20 m. The superconducting magnets were aligned to better than  $100\ \mu\text{m}$  and the normal conducting quadrupole magnets were aligned to better than 1 mm. In the other places, a survey is carried out using a total station which gives a spatial resolution of about 2 mm at a distance of 100 m.

We observed a ground sink of a few tens of millimeters during the construction stage. It was taken into account at the installation of the beamline components. After the installation at the primary beamline, we still observed a sink of several millimeters at the final focusing section and the target station. Therefore, the beam was tuned to follow the beamline sink.

The required directional accuracy from the physics point of view is  $1 \times 10^{-3}$  rad. The directional accuracy of a long baseline GPS survey is several times  $10^{-6}$  rad. That of a short distance survey is a few times  $10^{-5}$  rad. It was confirmed by surveys after construction that a directional accuracy of significantly better than  $1 \times 10^{-4}$  rad was attained.

The measured distance between the target and the center position of Super-Kamiokande is  $295,335.2 \pm 0.7$  m. The measured off-axis angle is  $2.504 \pm 0.004^\circ$ .

### 3.6.2. Time synchronization

The T2K GPS time synchronization system builds on experience from K2K, taking advantage of subsequent advances in commercially available clock systems and related technology. The system provides O(50 ns) scale synchronization between neutrino event trigger timestamps at Super-Kamiokande, and beam spill timestamps logged at J-PARC.

The heart of the system is a custom electronics board called the local time clock (LTC). This board uses a time base derived from a commercial rubidium clock, and references it to GPS time using input from two independent commercial GPS receivers. The operational firmware was coded to interface efficiently with the Super-Kamiokande or J-PARC data acquisition systems.

The LTC receives 1 pps (pulse per second) signals from two independent GPS receivers. These signals have their leading edges aligned with the second transitions in UTC to higher precision than required for T2K. The primary receiver is a TrueTime (Symmetricom) rack-mounted receiver, and the secondary receiver is a Synergy Systems SynPaQIII receiver, mounted as a daughtercard on the LTC itself. The receivers are connected to antenna modules located with a clear view of the sky, near the mine entrance at Super-Kamiokande, and at J-PARC. The Rb clock which provides a stabilized time base for the system in case of temporary loss of GPS signals is a Stanford Research Systems model FS-725. The LTC is interfaced to the data acquisition system through a Linux PC with fast network connections. At J-PARC, an independent optical fiber link sends data directly to the ND280 data acquisition system.

When the timing signal, synchronized with the MR extraction, is received its time is recorded to an LTC module at J-PARC. The LTC module counts the accumulated number of received signals as the spill number. This time information and the spill number are sent to Super-Kamiokande through a private network, and are returned from Super-Kamiokande to check consistency. The LTC module also provides the beam trigger for the beam monitors.

At each site, two independent GPS systems run in parallel at all times to eliminate downtime during T2K running.

## 4. Near detector complex (ND280)

As stated earlier, the T2K experiment studies oscillations of an off-axis muon neutrino beam between the J-PARC accelerator

complex and the Super-Kamiokande detector, with special emphasis on measuring the unknown mixing angle  $\theta_{13}$  by observing the subdominant  $\nu_\mu \rightarrow \nu_e$  oscillation. The neutrino energy spectrum, flavor content, and interaction rates of the unoscillated beam are measured by a set of detectors located 280 m from the production target, and are used to predict the neutrino interactions at Super-Kamiokande.

The primary detector at the 280 m site is a magnetized off-axis tracking detector. The off-axis detector elements are contained inside the magnet recycled from the UA1 experiment at CERN. Inside the upstream end of this magnet sits a pi-zero detector (PØD) consisting of tracking planes of scintillating bars alternating with either water target/brass foil or lead foil. Downstream of the PØD, the tracker, comprising three time projection chambers (TPCs) and two fine grained detectors (FGDs) consisting of layers of finely segmented scintillating bars, is designed to measure charged current interactions in the FGDs. The PØD, TPCs, and FGDs are all surrounded by an electromagnetic calorimeter (ECal) for detecting  $\gamma$ -rays that do not convert in the inner detectors, while the return yoke of the magnet is instrumented with scintillator to measure the ranges of muons that exit the sides of the off-axis detector. In addition to the off-axis detector, a separate array of iron/scintillator detectors called INGRID measures the on-axis neutrino beam profile at the 280 m site, while a set of muon monitor detectors located downstream of the beam dump monitors the beam direction and profile by detecting high energy muons from pion decay, as described earlier in Section 3.3. All detectors use the same coordinate convention:  $z$  is along the nominal neutrino beam axis, and  $x$  and  $y$  are horizontal and vertical, respectively.

These detectors are housed in a pit inside the ND280 hall (see Fig. 9). The pit has a diameter of 17.5 m and a depth of 37 m, and has three floors. The B1 floor, about 24 m below the surface, houses the off-axis detector, which is located on the line between the target point and the Super-Kamiokande position. The Service Stage, about 33 m deep, houses the horizontal modules of the INGRID detector. It also holds the electronics and many of the services for the off-axis detectors. The B2 floor, about 37 m deep, houses the bottom modules of the vertical INGRID detector. The current off-axis angle is  $2.5^\circ$ , which has the extrapolated on-axis beam passing at about 1 m above the Service Stage. This facility design can accommodate off-axis angles in the range of between  $2.0$  and  $2.5^\circ$ , constrained by the requirement that the beam axis pass through the central area of the on-axis detector. Outside of this area, the measurement of the beam axis direction would deteriorate. A building with an internal area of  $21\ \text{m} \times 28\ \text{m}$  covers the pit, and has a 10 ton crane.

### 4.1. Multi-pixel photon counter (MPPC)

The ND280 detectors make extensive use of scintillator detectors and wavelength-shifting (WLS) fiber readout, with light from the fibers being detected by photosensors that must operate in a magnetic field environment and fit into a limited space inside the magnet. Multi-anode PMTs, successfully used in other scintillator and WLS-based neutrino experiments, are not suitable for ND280 because most of the detectors in the ND280 complex have to work in a magnetic field of 0.2 T. To satisfy the ND280 experimental requirements, a multi-pixel avalanche photodiode was selected for the photosensor. The device consists of many independent sensitive pixels, each of which operates as an independent Geiger micro-counter with a gain of the same order as a vacuum photomultiplier. These novel photosensors are compact, well matched to spectral emission of WLS fibers, and insensitive to magnetic fields. Detailed information and the basic principles

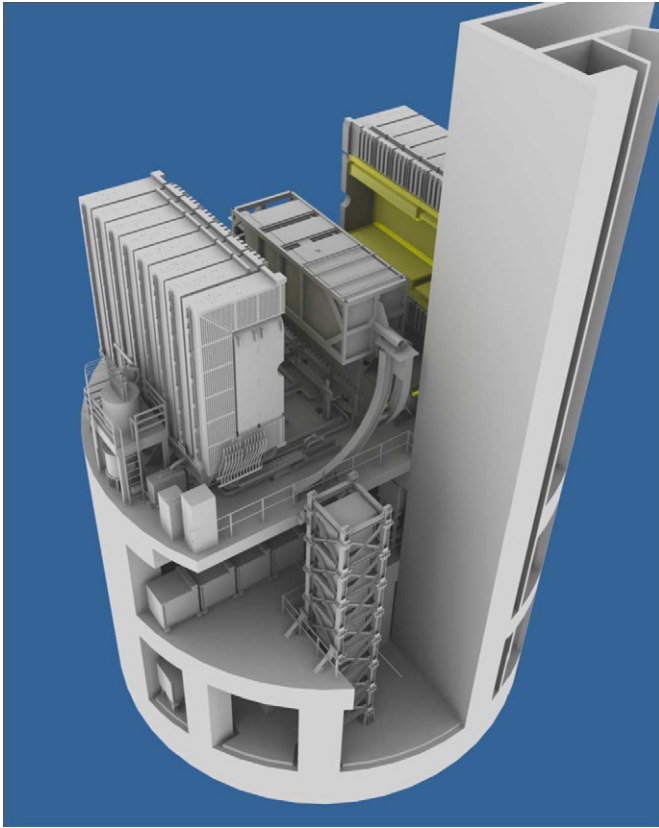


**Fig. 9.** ND280 detector complex. The off-axis detector and the magnet are located on the upper level; horizontal INGRID modules are located on the level below; and the vertical INGRID modules span the bottom two levels.

of operation of multi-pixel photodiodes can be found in a recent review paper [34] and the references therein.

After R&D and tests provided by several groups for three years, the Hamamatsu Multi-Pixel Photon Counter (MPPC) was chosen as the photosensor for ND280. The MPPC gain is determined by the charge accumulated in a pixel capacitance  $C_{\text{pixel}}$ :  $Q_{\text{pixel}} = C_{\text{pixel}} \cdot \Delta V$ , where the overvoltage  $\Delta V$  is the difference between the applied voltage and the breakdown voltage of the photodiode. For MPPCs the operational voltage is about 70 V, which is 0.8–1.5 V above the breakdown voltage. The pixel capacitance is 90 fF, which gives a gain in the range  $0.5\text{--}1.5 \times 10^6$ . When a photoelectron is produced it creates a Geiger avalanche. The amplitude of a single pixel signal does not depend on the number of carriers created in this pixel. Thus, the photodiode signal is a sum of fired pixels. Each pixel operates as a binary device, but the multi-pixel photodiode as a whole unit is an analog detector with a dynamic range limited by the finite number of pixels.

A customized 667-pixel MPPC, with a sensitive area of  $1.3 \times 1.3 \text{ mm}^2$ , was developed for T2K [35,36]. It is based on a Hamamatsu commercial device, the sensitive area of which was increased to provide better acceptance for light detection from 1 mm diameter Y11 Kuraray fibers. In total, about 64,000 MPPCs were produced for T2K. The T2K photosensor is shown in Fig. 10.

The main parameters of MPPCs are summarized in Table 2. The characterization of the MPPCs' response to scintillation light is presented in Ref. [37].

#### 4.2. INGRID on-axis detector

INGRID (Interactive Neutrino GRID) is a neutrino detector centered on the neutrino beam axis. This on-axis detector was

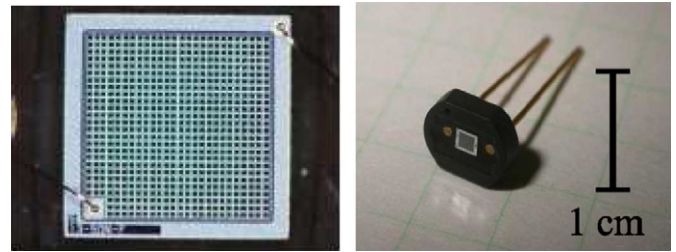


**Fig. 10.** Photographs of an MPPC with a sensitive area of  $1.3 \times 1.3 \text{ mm}^2$ : magnified face view (left) with 667 pixels in a  $26 \times 26$  array (a 9-pixel square in the corner is occupied by an electrode); the ceramic package of this MPPC (right).

**Table 2**

Main parameters of the T2K MPPCs.

Number of pixels	667
Active area	$1.3 \times 1.3 \text{ mm}^2$
Pixel size	$50 \times 50 \mu\text{m}^2$
Operational voltage	68–71 V
Gain	$\sim 10^6$
Photon detection efficiency at 525 nm	26–30%
Dark rate, threshold=0.5 p.e., $T=25^\circ\text{C}$	$\leq 1.35 \text{ MHz}$

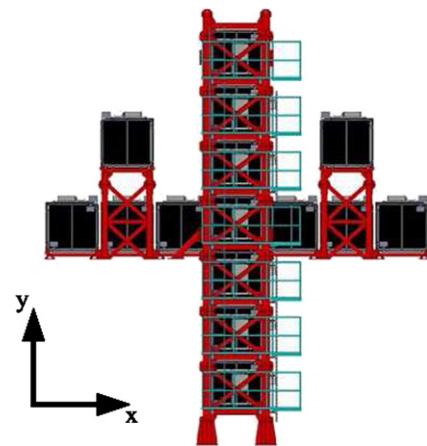


**Fig. 11.** INGRID on-axis detector.

designed to monitor directly the neutrino beam direction and intensity by means of neutrino interactions in iron, with sufficient statistics to provide daily measurements at nominal beam intensity. Using the number of observed neutrino events in each module, the beam center is measured to a precision better than 10 cm. This corresponds to 0.4 mrad precision at the near detector pit, 280 m downstream from the beam origin. The INGRID detector consists of 14 identical modules arranged as a cross of two identical groups along the horizontal and vertical axis, and two additional separate modules located at off-axis directions outside the main cross, as shown in Fig. 11. The detector samples the neutrino beam in a transverse section of  $10 \text{ m} \times 10 \text{ m}$ . The center of the INGRID cross, with two overlapping modules, corresponds to the neutrino beam center, defined as  $0^\circ$  with respect to the direction of the primary proton beamline. The purpose of the two off-axis modules is to check the axial symmetry of the neutrino beam. The entire 16 modules are installed in the near detector pit with a positioning accuracy of 2 mm in directions perpendicular to the neutrino beam.

The INGRID modules consist of a sandwich structure of nine iron plates and 11 tracking scintillator planes as shown in Fig. 12. They are surrounded by veto scintillator planes, to reject interactions

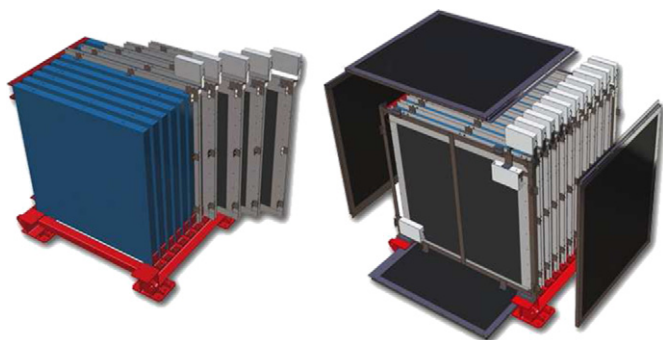


**Fig. 12.** An INGRID module. The left image shows the tracking planes (blue) and iron plates. The right image shows veto planes (black). (For interpretation of the references to color in this figure legend, the reader is referred to the web version of this article.)

outside the module. The dimensions of the iron plates are  $124\text{ cm} \times 124\text{ cm}$  in the  $x$  and  $y$  directions and  $6.5\text{ cm}$  along the beam direction. The total iron mass serving as a neutrino target is  $7.1\text{ tons}$  per module. Each of the 11 tracking planes consists of 24 scintillator bars in the horizontal direction glued to 24 perpendicular bars in the vertical direction with Cemedine PM200, for a total number of 8448. No iron plate was placed between the 10th and 11th tracking planes due to weight restrictions, but this does not affect the tracking performance. The dimensions of the scintillator bars used for the tracking planes are  $1.0\text{ cm} \times 5.0\text{ cm} \times 120.3\text{ cm}$ . Due to the fact that adjacent modules can share one veto plane in the boundary region, the modules have either three or four veto planes. Each veto plane consists of 22 scintillator bars segmented in the beam direction. The dimensions of those scintillator bars are  $1.0\text{ cm} \times 5.0\text{ cm} \times 111.9\text{ cm}$  (bottom sides) and  $1.0\text{ cm} \times 5.0\text{ cm} \times 129.9\text{ cm}$  (top, right and left sides). The total number of channels for the veto planes is 1144, which gives a total of 9592 channels for INGRID as a whole.

The extruded scintillator bars used for the tracking and veto planes are made of polystyrene doped with 1% PPO and 0.03% POPOP by weight. The wavelength of the scintillation light at the emission peak is  $420\text{ nm}$  (blue). They were developed and produced at Fermilab [38]. A thin white reflective coating, composed of  $\text{TiO}_2$  infused in polystyrene, surrounds the whole of each scintillator bar. The coating improves light collection efficiency by acting as an optical isolator. A hole with a diameter of about  $3\text{ mm}$  in the center of the scintillator bar allows the insertion of a WLS fiber for light collection.

The WLS fibers used for INGRID are  $1\text{ mm}$  diameter Kuraray double-clad Y-11. The absorption spectrum of the fiber is centered at a wavelength of  $430\text{ nm}$  (blue). The emission spectrum is centered at  $476\text{ nm}$  (green), and the overlap between the two is small, reducing self-absorption effects in the fiber. One end of the fiber is glued to a connector by epoxy resin (ELJEN Technology EJ-500). The surface of the connector was polished with diamond blades. An MPPC is attached to each fiber using the connector. A detailed description of the MPPCs can be found in Section 4.1. Some characterization of the MPPCs used for INGRID can be found in Refs. [36,39].

Finally, the set of scintillators, fibers and photosensors is contained in a light-tight dark box made of aluminum frames and plastic plates. The readout front-end electronics boards, the Trip-T front-end boards (TFBs), are mounted outside the dark box and each connected to 48 MPPCs via coaxial cables. This forms one complete tracking scintillator plane.

INGRID was calibrated using cosmic ray data taken on the surface and, during beam, in the ND280 pit. The mean light yield of each channel is measured to be larger than 10 photoelectrons per  $1\text{ cm}$  of MIP tracks which satisfies our requirement.

Furthermore, the timing resolution of each channel is measured to be  $3.2\text{ ns}$ .

An extra module, called the Proton Module, different from the 16 standard modules, has been added in order to detect with good efficiency the muons together with the protons produced by the neutrino beam in INGRID. The goal of this Proton Module is to identify the quasi-elastic channel for comparison with Monte Carlo simulations of beamline and neutrino interactions. It consists of scintillator planes without any iron plate and surrounded by veto planes. A different size scintillator bar was used to improve tracking capabilities. A schematic view of the Proton Module can be seen in Fig. 13. It is placed in the pit in the center of the INGRID cross between the standard vertical and horizontal central modules.

Typical neutrino events in the INGRID module and the Proton Module are shown in Figs. 14 and 15.

#### 4.3. Off-axis detector

A large fine grained off-axis detector (see Fig. 16) serves to measure the flux, energy spectrum and electron neutrino contamination in the direction of the far detector, along with measuring rates for exclusive neutrino reactions. This characterizes signals and backgrounds in the Super-Kamiokande detector.

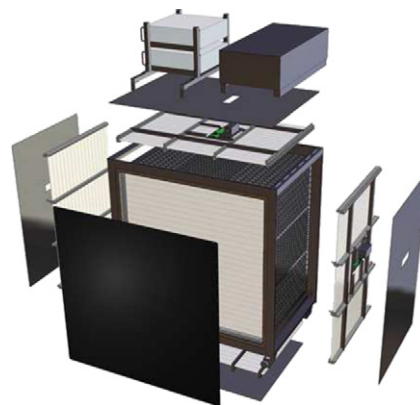


**Fig. 13.** The Proton Module. Similar to the INGRID modules, but with finer grain scintillator and without the iron plates.

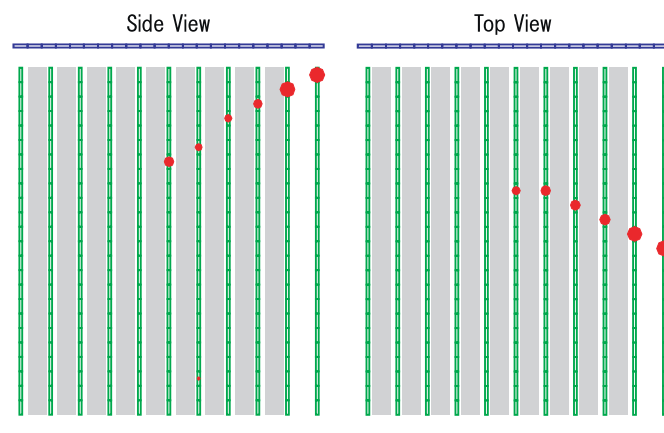


**Fig. 14.** A typical neutrino event in an INGRID module. A neutrino enters from the left and interacts within the module, producing charged particles. One of them makes a track which is shown as the red circles. Each of the green cells in this figure is a scintillator, and the size of the red circles indicates the size of the observed signal in that cell. Blue cells and gray boxes indicate veto scintillators and iron target plates, respectively. (For interpretation of the references to color in this figure legend, the reader is referred to the web version of this article.)

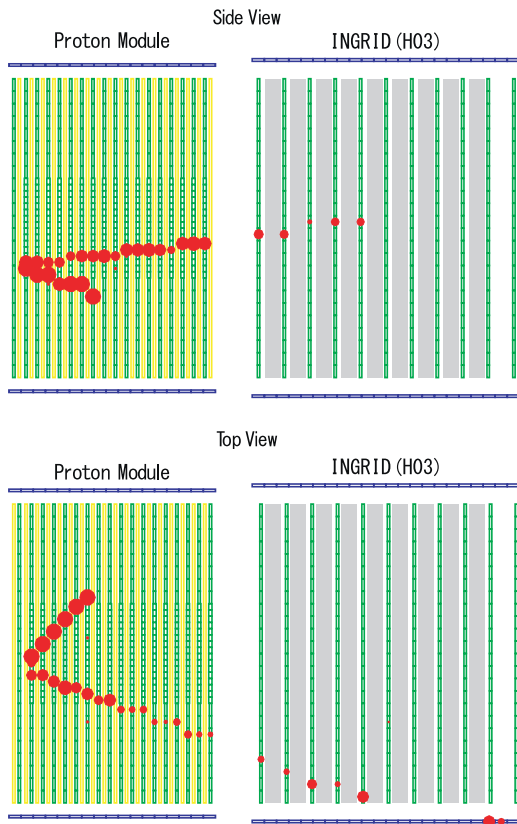


**Fig. 15.** A typical neutrino event in the Proton Module. A neutrino enters from the left and interacts within the module, producing charged particles whose tracks are shown as the red circles. One of them exits the Proton Module and enters the central INGRID horizontal module. Each of the green cells in this figure is a scintillator, and the size of the red circles indicates the size of the observed signal in that cell. Blue cells indicate veto scintillators. (For interpretation of the references to color in this figure legend, the reader is referred to the web version of this article.)

The ND280 off-axis detector must satisfy several requirements. Firstly, it must provide information to determine the  $\nu_\mu$  flux at the Super-Kamiokande detector. Secondly, the  $\nu_e$  content of the beam must be measured as a function of neutrino energy. The beam  $\nu_e$  background is expected to be approximately 1% of the  $\nu_\mu$  flux and creates a significant non-removable background. Thirdly, it must measure  $\nu_\mu$  interactions such that the backgrounds to the  $\nu_e$  appearance search at Super-Kamiokande can be predicted. These backgrounds are dominated by neutral current single  $\pi^0$  production. To meet these goals the ND280 off-axis detector must have the capability to reconstruct exclusive event types such as  $\nu_\mu$  and  $\nu_e$  charged current quasi-elastic, charged current inelastic, and neutral current events, particularly neutral current single  $\pi^0$  events. In addition, the ND280 off-axis detector should measure inclusive event rates. All of these requirements were considered in designing the off-axis detector.

The constructed off-axis detector consists of: the PØD and the TPC/FGD sandwich (tracker), both of which are placed inside of a metal frame container, called the “basket”; an electromagnetic calorimeter (ECAL) that surrounds the basket; and the recycled UA1 magnet instrumented with scintillator to perform as a muon range detector (SMRD). (See Fig. 16).

The basket has dimensions of 6.5 m × 2.6 m × 2.5 m (length × width × height). It is completely open at the top, to allow the insertion of the various detectors. Two short beams are fixed at the center of the two faces of the basket perpendicular to the beam axis. The short beam at each end of the basket connects to

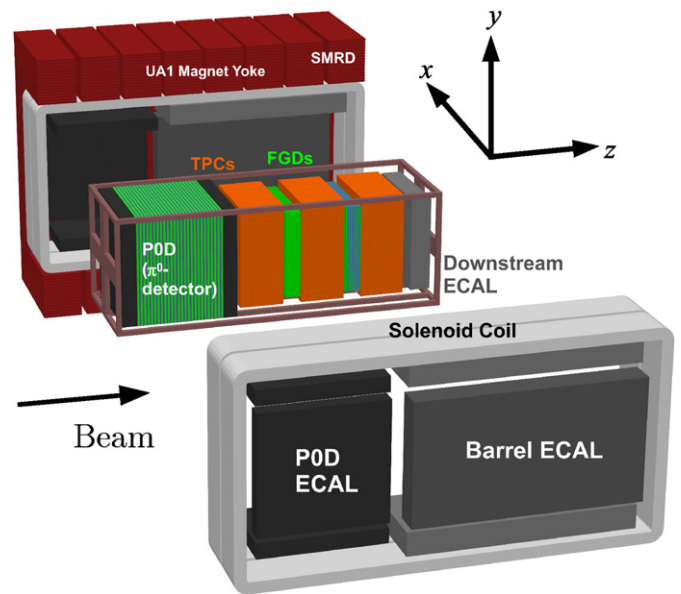


**Fig. 16.** An exploded view of the ND280 off-axis detector.

an axle which runs through the hole in the magnet coil originally intended to allow passage of the beam pipe in the UA1 experiment. The axle is in turn supported by an external support frame which is bolted to the floor. When opening the magnet, the half yokes and the coils move apart, while the basket and the inner detector remain fixed in the position chosen for data taking. In the following sections, more detailed descriptions of these elements are provided.

#### 4.3.1. UA1 magnet

The ND280 off-axis detector is built around the old CERN UA1/NOMAD magnet providing a dipole magnetic field of 0.2 T, to measure momenta with good resolution and determine the sign of charged particles produced by neutrino interactions.

The magnet consists of water-cooled aluminum coils, which create the horizontally oriented dipole field, and a flux return yoke. The dimensions of the inner volume of the magnet are 7.0 m × 3.5 m × 3.6 m. The external dimensions are 7.6 m × 5.6 m × 6.1 m and the total weight of the yoke is 850 tons. The coils are made of aluminum bars with 5.45 cm × 5.45 cm square cross sections, with a central 23 mm diameter bore for water to flow. The coils are composed of individual “pancakes” which are connected hydraulically in parallel and electrically in series.

The magnet consists of two mirror-symmetric halves. The coils are split into four elements, two for each half, and are mechanically supported by, but electrically insulated from, the return yoke. The two half yoke pieces each consist of eight C-shaped elements, made of low-carbon steel plates, which stand on movable carriages. The carriages are fitted on rails and operated by hydraulic movers, so that each half magnet is independent of the other and can be separately moved to an open or closed position. When the magnet is in an open position, the inner volume is accessible, allowing access to the detectors.

The magnet yoke and coils were reused from UA1/NOMAD, while the movers were obtained from the completed HERA-B experiment at DESY. In order to comply with seismic regulations, detailed FEM static and dynamic analyses were performed and cross-checked with measurements of deformation and modal frequency of the yoke elements. As a result of this, the carriages were mechanically reinforced by additional steel bars to increase

their lateral strength. Additional components had to be specially designed and built for the ND280 magnet operation. These were: the power supply (PS), the cooling system (CS), the magnet safety system (MSS), and the magnet control system (MCS). Finally, the magnetic field map was determined *in situ* with a dedicated measurement campaign.

The PS, specially made for ND280, was designed and manufactured by Bruker to provide the DC current to energize the magnet. The nominal current is 2900 A with a voltage drop of 155 V. The requirements for the DC current resolution and stability were 300 ppm and  $\pm 1000$  ppm over 24 h, respectively. The PS is also able to cope with AC phase imbalance ( $\pm 2\%$ ) and short voltage drops. A thyristor switch mode was employed, with digital current regulation via a DCCT captor (ULTRASTAB series from Danfysik). The power supply can be controlled locally or remotely via the MCS.

The CS, assembled by MAN Ferrostaal AG (D), provides up to 750 kW of cooling power via two independent demineralized water circuits to compensate for the heat loss from the coils and in the power supply. The cold source consists of a primary glycol circuit maintained at 8 °C by a chiller (built by FrioTherm, D). The secondary pumping circuit units and their heat exchangers, the water purification units and the main panel controller are mounted in an ISO container, suitable for easy road and sea transport. They were assembled and tested in Europe before shipment to J-PARC. The secondary circuit demineralized water for the magnet coils has a flow of 30 L/s and a pressure of 10 bar to compensate for the 7 bar pressure drop across the coil bore holes.

The MSS, based on a hardwired fail-safe interface, was built to ensure the operational safety of the magnet. It continuously monitors a set of input signals from the thermo-switches mounted on the magnet coils, fault signals from the power converter, cooling and magnet control systems, and magnet emergency stop signals from manual buttons located in the ND280 building. A Boolean OR of all fault signals is generated and logically combined with the on/off magnet status. When the magnet is off, the system issues a power convert permit signal only if none of the input signals is in a fault state. When the magnet is operating, a fast abort signal is generated and sent to the power converter in less than 1 ms when any of the input signals switches to a fault state. All input and output signals of the MSS are monitored by a VME computer, and any change in the status of the signals is recorded with 1 ms timing resolution, meaning that the detailed sequence of events leading up to a fast abort can be understood.

The aim of the MCS is to monitor the behavior of the magnet and cooling system, to control the current set point of the magnet power supply and to interface all the information and control parameters with the global slow control (GSC). The system is based on an industrial programmable logic controller (PLC) that reads: the coil temperature at 52 points; the water flow, input and output temperature and pressure on each half of the magnet; the voltage drop through each half of the magnet; the power converter voltage and current; and the status flags of the power converter, CS and MSS. The PLC is linked via PROFIBUS DP (Process Field Bus for Decentralized Peripherals) with the power converter, in order to switch on and off, and to read and write, the current and other settings. All this information is processed and analyzed several times per second. If any subsystem should exceed the operational parameters, the MCS will switch off the magnet and trigger the corresponding alarms for later diagnostics. All the information in the PLC can be accessed via an open connectivity standard for industrial automation (OPC server). The OPC server is interfaced with the GSC for monitoring and control of the magnet. The measured current is used offline to define the magnetic field for data analysis.

The refurbishing of the magnet yokes and aluminum coils was performed at CERN. Then, they were packed and shipped to Japan,

and reassembled and installed in the ND280 pit. During the installation particular attention was paid to take into account the constraints of alignment coming from the later insertion of the SMRD modules within the gaps of the magnet yokes, which required that the 16 individual yoke elements, each weighing 53 tons, be aligned with a precision of better than 1 mm. After successful magnet yoke and coil assembly, the installation of the services was performed. In August 2009 the B-field mapping device was installed in the basket and the magnet was then ready to be closed. The commissioning and B-field mapping procedure during August/September 2009 allowed for comprehensive testing of many aspects of the magnet.

During the dedicated mapping procedure the magnetic field of the ND280 magnet was precisely measured with a computer-controlled movable device equipped with 89 electronic cards, each holding three orthogonal Hall probes and the corresponding readout electronics. The overall mechanical structure of the device had dimensions of  $2\text{ m} \times 2\text{ m} \times 1\text{ m}$  and could be moved throughout the whole instrumented region of the basket. Special care was taken in the region of the TPCs. The intrinsic uncertainty of each Hall probe in our region of interest is 0.2 G and the systematic error of the measurements is as low as 0.5 G. This was ensured by a calibration method employing a very well-known homogeneous field, from a magnet designed for the purpose. Higher-order magnetic moments and second-order Hall effects were taken into account for the measurements.

An important element of the field mapping was surveying the position and skewing of the measurement device before, during, and after the mapping. Two surveys were carried out. One related the reference frame of the mapping machine to the ND280 main reference frame; the accuracy of this survey is better than 1 mm in position offset and better than 1 mrad in rotational uncertainty. The second survey defined the internal reference frame of the mapping device, which is even more accurate, with the possibility of measuring changes in position up to a precision of 10  $\mu\text{m}$ . The alignment of the Hall probes with respect to each other was ensured at a level of 1 mrad. The above-mentioned systematic error of 0.5 G was achieved by exploiting the ND280 magnet's Cartesian symmetry.

The measurements were performed at a magnetic field value of 0.07 T—lower than the nominal field during neutrino data taking due to limited electrical power available at the time from the ND280 facility. It was therefore necessary to rescale to the nominal field, also taking hysteresis and saturation effects into account. By using a quadratic function as a first-order correction, a field uncertainty of  $10^{-3}$  was obtained after scaling. The errors of the measurements scale in the same way, leading to a final magnetic field uncertainty of 2 G for each field component at the nominal field of 0.2 T. This very precise knowledge of the magnetic field map, especially for the transverse field components, helps to reduce the systematic uncertainty of the momentum determination, which is intended to be below 2% for charged particles below 1 GeV/c.

Figs. 17 and 18 show two performance plots of the magnetic field mapping. Fig. 17 shows a slice of the TPC region. The field is quite homogeneous in the center of the magnet but increasingly varies the closer one comes to the edges of the TPC region. In Fig. 18, the difference between our fit to the data and the actual measured values is plotted for each B-field component. The widths of the resulting distributions are a measure of the systematic error of the B-field measurement. They indicate residuals less than 1 G for each field component.

#### 4.3.2. Pi-zero detector (P0D)

The primary objective of the P0D is to measure the neutral current process  $\nu_\mu + N \rightarrow \nu_\mu + N + \pi^0 + X$  on a water ( $\text{H}_2\text{O}$ ) target with the same neutrino beam flux as reaches Super-Kamiokande.

These aims were realized by a design using  $x$  and  $y$  planes of scintillator bars, with each bar read out with a single WLS fiber. The planes of scintillator bars are interleaved with fillable water target bags and lead and brass sheets. This arrangement forms a neutrino target where the PØD operates with the water target bags filled or emptied, enabling a subtraction method to determine the water target cross sections. The scintillator bars provide sufficiently fine segmentation to reconstruct charged particle tracks (muons and pions) and electromagnetic showers (electrons and photons from  $\pi^0$ 's).

The main features of the PØD design are shown in Fig. 19. The central section, composed of the “upstream water target” and “central water target”, uses alternating scintillator planes, HDPE water bags, and brass sheets. The front and rear sections, the “upstream ECal” and “central ECal”, use alternating scintillator planes and lead sheets. This layout improves the containment of electromagnetic showers and provides a veto region before and after the water target region to provide effective rejection of particles entering from interactions outside the PØD.

There are a total of 40 scintillator modules in the PØD. Each PØD module, or PØDule, has two perpendicular arrays of triangular

scintillator bars. There are 134 vertical bars (2200 mm long) and 126 horizontal bars (2340 mm long) in each PØDule. Each bar has a single hole filled with a WLS fiber (Kuraray double-clad Y11 of 1 mm diameter). Each fiber is mirrored on one end and the other end is optically read out using a Hamamatsu MPPC (see Section 4.1). Each photodetector is read out with TFB electronics (see Section 4.4). There are 40 PØDules, each with 260 scintillator bars and fibers being read out, totaling 10,400 channels for the entire PØD detector. The PØDules were formed into four “super-groups” called super-PØDules. The two ECal super-PØDules are a sandwich of seven PØDules alternating with seven stainless steel clad lead sheets (4 mm thick). The upstream (central) water target

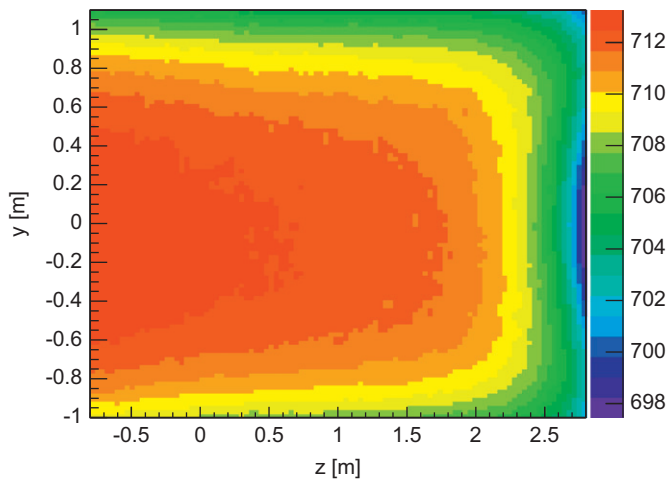


**Fig. 17.** The color plot shows a slice ( $x=0$ , the basket central plane) of the mapped B-field (in Gauss) in the TPC region. The neutrino beam is entering the picture from the left. (For interpretation of the references to color in this figure legend, the reader is referred to the web version of this article.)

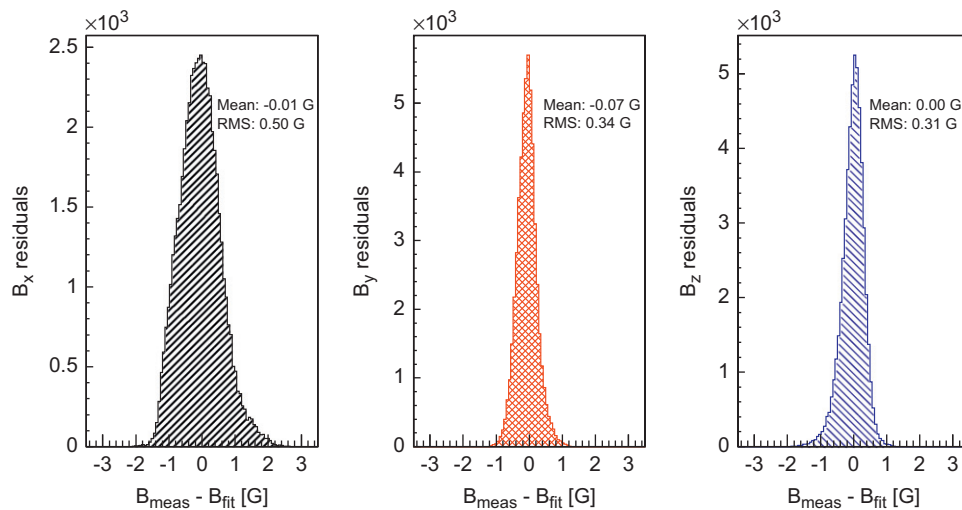


**Fig. 18.** For each B-field component ( $x$ ,  $y$  and  $z$ , respectively) the residuals between a fit of the data and the actual measurements is shown. The RMS of the distributions is taken as a measure of the systematic uncertainty of the mapping. The fit is performed in the center region.

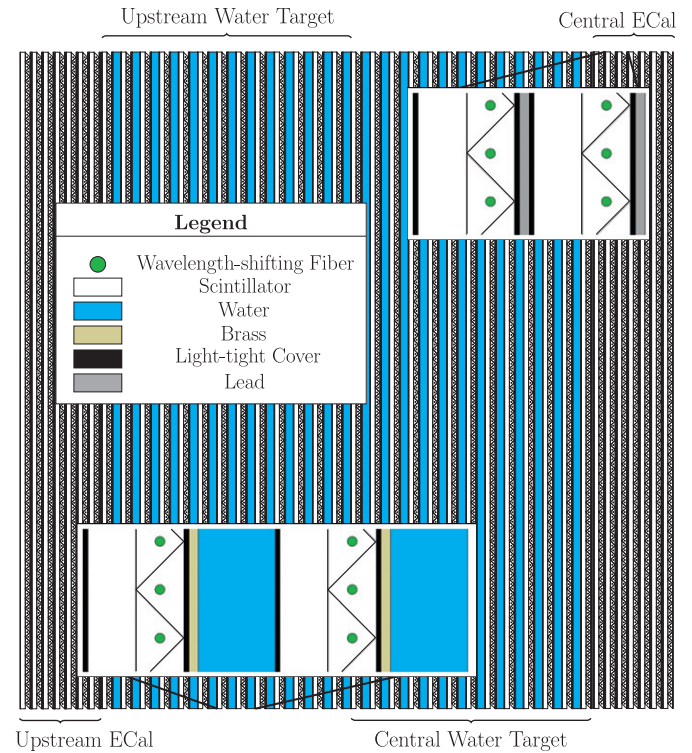


**Fig. 19.** A schematic of the pi-zero detector. The beam is coming from the left and going right. Insets show details of the Water Target super-PØDule layers and Central ECal layers.

super-PØDule is a sandwich of 13 PØDules alternating with 13 (12) water bag layers (each 28 mm thick), and 13 (12) brass sheets (each 1.5 mm thick). The water target layers each have two bags, for a total of 50 in the PØD detector, each with dimensions of 1006 mm × 2062 mm × 28 mm. The dimensions of the active target of the entire PØD are 2103 mm × 2239 mm × 2400 mm (width × height × length) and the mass of the detector with and without water is 16.1 and 13.3 tons, respectively.

The PØD polystyrene scintillator bars were identical to bars originally developed for the MINERvA experiment [40]. The bulk polystyrene is Dow Styron 663 (W), a commercial grade, general-purpose polystyrene without additives. Wavelength-shifting dopants, 1% PPO and 0.03% POPOP, were added into the bulk polystyrene. The cross section of the extrusion is an isosceles triangle with a 33 mm base and 17 mm height. There is a hole centered in both dimensions, with a diameter of approximately 1.5 mm, through which a WLS fiber may be inserted. A thin (0.03 mm on average) co-extruded layer of polystyrene with 20% TiO<sub>2</sub> was added to the outside of the strip in order to reflect escaping light back into the bulk and increase the probability of capture by the center fiber.

The WLS fibers were mounted in the scintillating bars by gluing a custom ferrule over one end of each fiber so that a small portion of the fiber and epoxy extended past the ferrule. The fiber and epoxy were then diamond-polished. The MPPCs were mounted in custom sleeves designed to snap-fit to a ferrule, allowing them to be installed and removed as necessary.

The PØD construction was done in three stages. First, the scintillator bars were glued into arrays of 15–17 bars on a template mounted on an optical table. The arrays were cured at room temperature, under a vacuum film, for a minimum of four hours. These pre-glued bar arrays were called “planks”. Each PØDule uses 16 planks and a total of 640 are required for the entire detector.

In the next stage, the PØDules were constructed on a gluing table. The PØDules were assembled as a sandwich of an outer lower PVC skin, eight *x*-scintillator planks, eight *y*-scintillator planks, and an outer upper PVC skin. All four edges of the assembly were enclosed with PVC frames, which had been drilled with precision holes to allow the fibers to be inserted and connected to the MPPCs after the PØDules were assembled. The assembly was coated with epoxy and cured under a vacuum film overnight. After the PØDules were assembled, the fibers were inserted into each bar, and the MPPCs were attached to the fibers and connected via mini-coaxial cables to the TFB electronics boards. Then the PØDule was scanned with a movable <sup>60</sup>Co source to characterize the signal from every channel.

In the last stage, the instrumented PØDules were assembled into super-PØDules by laying a PØDule with lead plates (for the ECals) or water bags plus brass sheets (for the water targets) on a horizontal strongback table. This strongback table was lifted to a vertical position to assemble an upright super-PØDule. Finally, the TFB electronics boards were mounted onto aluminum plates attached to two aluminum cooling extrusions in which a closed loop of negative-pressure cooling water flows at ~ 5 L/min. The electronics plus cooling assembly was mounted on the top and one side of the super-PØDule. A light injection system was added that strobes the opposite end of the fiber with an LED flasher. Final testing of the super-PØDules, using a cosmic ray trigger, the water bag filling system and the light injection system, was done at J-PARC, prior to installation into the ND280 off-axis detector.

After installation of the super-PØDules in the pit, airtight aluminum cover panels were placed over the electronics and dry air was circulated to moderate temperature fluctuations while preventing condensation on the electronics cooling system.

Determining the amount of water in the fiducial volume is critical to the PØD physics goals. The required precision is

achieved by first measuring the mass vs. depth in an external buffer tank, filling the water targets to predetermined levels, and then observing the water volume removed from the tank. The water target volume is instrumented using a combination of binary (wet or dry) level sensors and pressure sensors, allowing the depth of the water to be determined to ± 5 mm. The water target fiducial region is designed to contain 1944 ± 53 kg of water, and the measured mass is 1902 ± 16 kg.

During initial operations, all but seven of the 10,400 PØD detector channels were operational. The detector was calibrated with minimum ionizing tracks from cosmic ray muons. An average of 19 photoelectrons was obtained for the scintillator bars and 38 photoelectrons per *x/y* layer. The average attenuation of the pulse height in the scintillator bars from opposite ends is approximately 30%. The internal alignment of scintillator bars was checked using through-going muons with the magnet field off, and was determined to be approximately 3 mm.

#### 4.3.3. Time projection chamber (TPC)

The TPCs perform three key functions in the near detector. Firstly, with their excellent imaging capabilities in three dimensions, the number and orientations of charged particles traversing the detectors are easily determined and form the basis for selecting high purity samples of different types of neutrino interactions. Secondly, since they operate in a magnetic field, they are used to measure the momenta of charged particles produced by neutrino interactions elsewhere in the detector, and, therefore, determine the event rate as a function of neutrino energy for the neutrino beam, prior to oscillation. Finally, the amount of ionization left by each particle, when combined with the measured momentum, is a powerful tool for distinguishing different types of charged particles, and in particular allows the relative abundance of electron neutrinos in the beam to be determined.

Each TPC consists of an inner box that holds an argon-based drift gas, contained within an outer box that holds CO<sub>2</sub> as an insulating gas. The inner (outer) walls are made from composite panels with copper-clad G10 (aluminum) skins. The inner box panels were precisely machined to form an 11.5 mm pitch copper strip pattern which, in conjunction with a central cathode panel, produces a uniform electric drift field in the active drift volume of the TPC, roughly aligned with the field provided by the near detector magnet. A simplified drawing of the TPC design is shown in Fig. 20.

Charged particles passing through the TPCs produce ionization electrons in the gas that drift away from the central cathode and toward one of the readout planes. There, the electrons are multiplied and sampled with bulk micromegas [41] detectors with 7.0 mm × 9.8 mm (vertical × horizontal) anode pad segmentation. The pattern of signals in the pad plane and the arrival time of the signals combine to give complete 3D images of the paths of the traversing charged particles. Twelve 342 mm × 359 mm micromegas modules tile each readout plane, for a total of 72 modules and nearly 9 m<sup>2</sup> of active surface for the three TPCs, the first to use micropattern gas detectors in a physics experiment. The modules are arranged in two vertical columns that are offset so that the small inactive regions between modules are not aligned.

Blind vias are used to route connections between the readout pads and connectors on the back side of the micromegas printed circuit boards. Six front-end electronics cards, each using four custom ASICs called “AFTER”, plug into the connectors and sample and digitize signals from the 1728 pads. Each AFTER ASIC shapes the signals and buffers 72 pad signals into 511 time-bin switched capacitor arrays. The six front-end cards connect to a single front-end mezzanine card

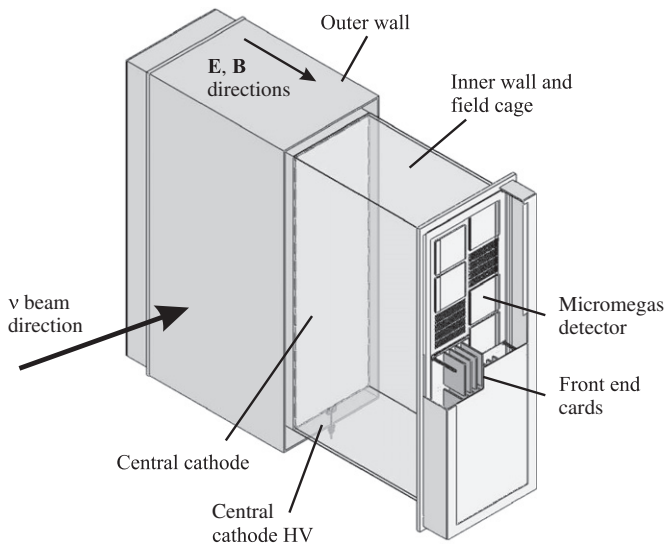


**Fig. 20.** Simplified cut-away drawing showing the main aspects of the TPC design. The outer dimensions of the TPC are approximately 2.3 m × 2.4 m × 1.0 m.

that aggregates the data, performs zero suppression, and sends the remaining data off detector over a 2 Gb/s optical link.

The gas system was designed to maintain a stable mixture in the inner volume, a constant positive pressure with respect to the outer volume, and a constant pressure between the outer volume and the atmosphere. The inner gas mixture, Ar:CF<sub>4</sub>:iC<sub>4</sub>H<sub>10</sub> (95:3:2) was chosen for its high speed, low diffusion, and good performance with micromegas chambers. Each of the three TPC volumes contains 3000 l, and each of the three gap volumes contains 3300 l. The TPC gas system was designed for an operating flow of 10 L/min/TPC (30 L/min total flow), corresponding to five TPC-volume flushes per day. To reduce gas operating costs, the system was designed to purify and recycle roughly 90% of the TPC exhaust gas.

A calibration system produces a control pattern of electrons on the central cathode in order to measure and monitor important aspects of the electron transport in the TPCs. Photoelectrons are produced from thin aluminum disks glued to the copper surface of the cathode by flashing the cathode with a diffuse pulse of 266 nm light. Data from this system are used to precisely determine the electron drift velocity and to measure distortions in the electron drift due to inhomogeneous and misaligned electric and magnetic fields.

Since late 2009, the three TPCs have been in place within the off-axis near detector, and the TPC systems operated stably during the first physics run. After correcting for atmospheric pressure variation, the residual gain variation, due to other factors such as gas composition, is below 1% and, therefore, does not degrade particle identification performance.

Particle identification is done with a truncated mean of measurements of energy loss of charged particles in the gas. The linear charge density of the track is estimated for each cluster by taking into account the length of the track segment corresponding to a pad column. The lowest 70% of the values are used to compute the truncated mean, an optimized approach found through Monte Carlo simulation and test beam studies. The resolution of deposited energy obtained using this method is about 7.8% for minimum ionizing particles, better than the design requirement of 10%. Fig. 21 demonstrates the TPC particle identification capability by comparing energy loss and momentum for positively charged particles recorded during the first T2K physics run.

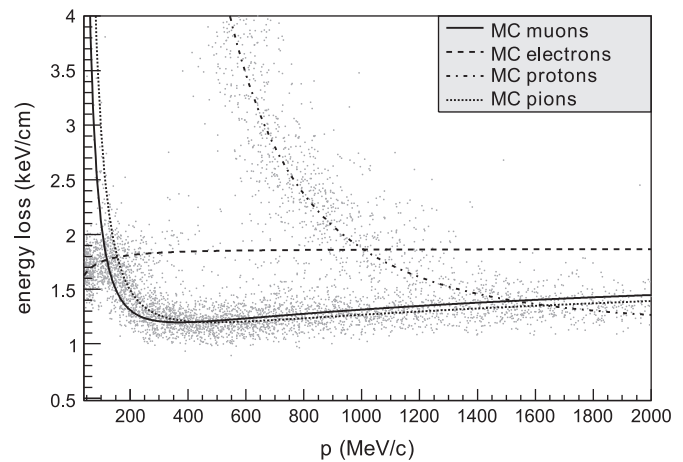


**Fig. 21.** Each point shows measurements by a single TPC of the energy loss and momentum of positively charged particles produced in neutrino interactions. The expected relationships for muons, positrons, protons, and pions are shown by the curves.

The point spatial resolution is estimated by comparing the transverse coordinate resulting from the global track fit to the one obtained with information from a single column of pads. The resolution is found to be typically 0.7 mm per column, in line with expectations, and degrades with increasing track angle with respect to the horizontal due to the ionization fluctuations along the track. The observed spatial resolution is sufficient to achieve the momentum resolution goals for the detectors.

More information about the design, construction, and performance of the TPC systems can be found in a recent publication [42].

#### 4.3.4. Fine grained detector (FGD)

Two fine grained detectors (FGDs) provide target mass for neutrino interactions as well as tracking of charged particles coming from the interaction vertex. The FGDs are constructed from 9.61 mm × 9.61 mm × 1864.3 mm bars of extruded polystyrene scintillator, which are oriented perpendicular to the beam in either the x or y direction. Each scintillator bar has a reflective coating containing TiO<sub>2</sub> and a WLS fiber going down a hole in its center. One end of each fiber is mirrored by vacuum deposition of aluminum, while the other end is attached to an MPPC and associated electronics, which digitize the light signal produced by scintillation inside the bar.

Each FGD (see Fig. 22) has outer dimensions of 2300 mm × 2400 mm × 365 mm (width × height × depth in beam direction), and contains 1.1 tons of target material. The first FGD consists of 5760 scintillator bars, arranged into 30 layers of 192 bars each, with each layer oriented alternately in the x and y directions perpendicular to the neutrino beam. The scintillator provides the target mass for neutrino interactions, and having alternating x and y layers of fine grained bars allows for tracking of charged particles produced in those interactions. An “XY module” consists of one layer of 192 scintillator bars in the horizontal direction glued to 192 perpendicular bars in the vertical direction, with thin G10 sheets glued to the outer surfaces to add structural stability. The photosensors are mounted along all four sides of the XY module on photosensor bus-boards that are screwed directly into the edges of the XY module. Each fiber is read out from one end, and within an x or y layer alternating fibers are read out from alternating ends. An LED-based light injection system that flashes the exposed far ends of the WLS fibers permits *in situ* calibration of photosensor response, saturation, and non-linearity.

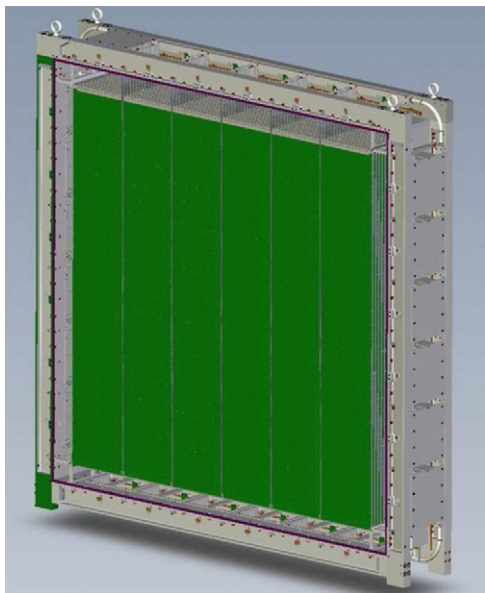


**Fig. 22.** View of an FGD with the front cover removed. XY scintillator modules (green) hang perpendicular to the direction of the neutrino beam. Along the top, six mini-crates with electronics can be seen without their cooling lines, while on the right side the cooling lids covering the mini-crates are shown. (For interpretation of the references to color in this figure legend, the reader is referred to the web version of this article.)

The second FGD is a water-rich detector consisting of seven XY modules of plastic scintillator alternating with six 2.5 cm thick layers of water (for a total of 2688 active scintillator bars and 15 cm total thickness of water). These layers are made from sheets of thin-walled hollow corrugated polycarbonate, 2.5 cm thick, whose ends have been sealed with HE 1908 polyurethane sealant. The modules are then filled with water to provide a layer of water target. The water is maintained under sub-atmospheric pressure by a vacuum pump system so that if a leak develops the system will suck air into the modules rather than spilling water inside the FGD. Comparing the interaction rates in the two FGDs permits separate determination of cross sections on carbon and on water.

Both FGDs were built with the same geometry, mounting, and readout for interoperability. Each FGD is contained in a light-tight dark box that contains the scintillator, fibers, and photosensors, while the FGD electronics are mounted in mini-crates around the outside of the dark box. The modules are supported by several stainless steel straps that loop around the bottom of each module and attach to anchor points in the top side of the dark box. The dark box itself is a sturdy aluminum frame that supports the weight of the FGD modules and transfers that weight to the detector basket. The walls of the dark box are made of thin opaque panels to keep its interior light-tight.

The FGD's front-end electronics resides in 24 mini-crates that attach to the outside of the four sides of the dark box. Signals from the photosensors inside the dark box are carried from the photosensor bus-boards to the electronics by ribbon cables that attach to the crates' backplanes, which are mounted over cutouts on the four sides of the box. The mini-crates are cooled by a negative-pressure water cooling system running along the sides of the frame of the dark box, and power is carried to the mini-crates by a power bus mounted on the frame. The electronics is arranged so that all heat-producing elements are located outside of the dark box in the mini-crates where they can be readily cooled by the cooling system, while only elements with negligible power outputs (the photosensors themselves) are present inside the dark box.

Each mini-crate contains four front-end boards and one crate master board (CMB), and can read out 240 photosensors. The front-end boards use the "AFTER" ASIC (Section 4.3.3), to shape and digitize high and low attenuation copies of the photosensor signals at 50 MHz, storing the waveform in a 511-deep switched capacitor array. In addition the front-end boards provide the photosensor bias voltages and analog trigger primitives. Data from each crate is read out over optical fiber links to data collector cards (DCCs) located outside of the magnet. Slow control systems use a separate data and power bus for redundancy.

#### 4.3.5. Electromagnetic calorimeter (ECal)

The ND280 ECal is a sampling electromagnetic calorimeter surrounding the inner detectors (PØD, TPCs, FGDs). It uses layers of plastic scintillator bars as active material with lead absorber sheets between layers, and it provides near-hermetic coverage for all particles exiting the inner detector volume. Its role is to complement the inner detectors in full event reconstruction through the detection of photons and measurement of their energy and direction, as well as the detection of charged particles and the extraction of information relevant for their identification (electron–muon–pion separation). A key function of the ECal is the reconstruction of  $\pi^0$ 's produced in neutrino interactions inside the tracker detectors. In the case of  $\pi^0$  production inside the PØD, the PØD-ECal complements the PØD reconstruction with information on escaping energy.

The ECal is made of 13 independent modules of three different types arranged as in Fig. 16: six Barrel-ECal modules surround the tracker volume on its four sides parallel to the  $z$  (beam) axis; one downstream module (Ds-ECal) covers the downstream exit of the tracker volume; and six PØD-ECal modules surround the PØD detector volume on its four sides parallel to the  $z$  axis. Each module is made of consecutive layers of scintillator bars glued to a sheet of lead converter. The Ds-ECal is located inside the basket carrying the inner subdetectors of the off-axis detector. The other 12 ECal modules are mounted inside of the UA1 magnet. A drawing of a completed module is shown in Fig. 23.

All ECal scintillator bars have a  $4.0\text{ cm} \times 1.0\text{ cm}$  cross section with a  $2.0\text{ mm} \times 3.0\text{ mm}$  elliptical hole running along their full length in the middle. The bars were extruded at a dedicated Fermilab facility and the material used was polystyrene doped with 1% PPO and 0.03% POPOP. A 0.25 mm thick layer of  $\text{TiO}_2$  was

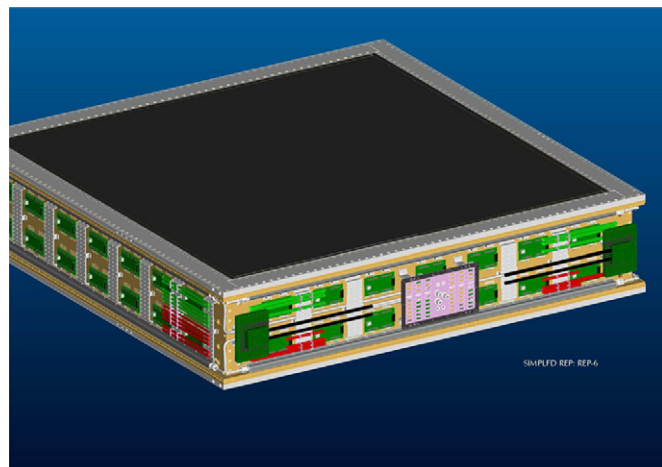


**Fig. 23.** External view of one ECal module. The scintillator bars run horizontally inside the module as shown. The readout electronics, signal and power cables, and cooling pipes can be seen mounted on the aluminum plates on the sides of the module. The gray surface at the top is the carbon fiber sandwich front plate, which in the final module position is facing towards the inner subdetectors (PØD, FGDs and TPCs).

co-extruded at the surface of the bars providing light reflection and isolation. A Kuraray 1 mm diameter double-clad Y11 WLS fiber runs along the hole in the center of each bar as described in Section 4.2 for the INGRID. The fibers were cut to length and diamond-polished at a dedicated Fermilab facility. The light is read out at one or both ends of each fiber with MPPCs (see Section 4.1). Those read out at one end only are mirrored at the other end with vacuum deposition of aluminum, performed at the same facility. Fiber-MPPC optical coupling is achieved using custom-made plastic connector assemblies. A ferrule is glued to the fiber end using Saint-Gobain BC600 silicon-based epoxy resin. The ferrule secures mechanically inside an MPPC holder that includes a layer of elastic foam to ensure good contact between the fiber end and the MPPC entrance window. The MPPC signal is read out with TFB cards (see Section 4.4). The lead sheets are made of lead with 2% antimony to provide some stiffness and were primed on both sides with a quick-drying metal primer.

Each ECal module was assembled from pre-made scintillator-lead layers. Each layer was prepared by laying the appropriate scintillator bars on a special aluminum tooling plate, aligning them within a border made of precision-machined aluminum bars, and gluing them to the lead sheets using Araldite 2011 cured for a few hours under vacuum bagging. For each module, the front of the mechanical frame is made of a carbon fiber sandwich front plate, which provides support while putting minimal material in the way of incoming photons, glued to an aluminum frame. The frame is screwed to side plates made of thick aluminum with holes to allow the WLS fibers to exit. Attached to the side plates are back frames made of aluminum plates which provide support and a system for securing the modules in their final position. A separate side wall made of thinner aluminum plates carries the TFB readout cards, special extruded pipes carrying cooling water, and a dry-air circulation system, and supports power distribution bars and signal and communication cables. Each complete module is closed off with thin aluminum covers for protection and light tightening.

For every module, the mechanical structure was assembled and aligned and then the scintillator-lead layers were installed one at a time. For each layer the fibers were threaded and glued to their ferrules. After the glue had cured, all fibers of the layer were connected to a test system of MPPCs and readout electronics of well-known performance and scanned with a  $^{137}\text{Cs}$  source moved along each bar in predefined spatial intervals. An automated scanner, data acquisition system and analysis software suite allowed this process to be completed within a few hours for each layer. In this manner, a very small percentage of fibers were found to be damaged; these were replaced before the next layer was installed in the module. Once all layers of each module were in place the module was fitted with the readout electronics, cables, and other services, tested, and shipped to J-PARC for installation.

The Ds-ECal module consists of 34 layers with lead sheets of 1.75 mm thickness for a total of  $10.6 X_0$ . There are 50 bars, each 2.04 m long, in every layer and each one is read out with an MPPC at each end. Consecutive layers have their bars at  $90^\circ$  to allow three-dimensional reconstruction of electromagnetic clusters and charged particle tracks.

Limited by available space inside the UA1 magnet and structural considerations, the Barrel-ECal modules have 31 layers each with the same lead sheets of 1.75 mm thickness for a total of  $9.7 X_0$ . Layers are again assembled with bar orientation alternating at  $90^\circ$ . The bars running in the  $z$  direction are 3.84 m long and are read by MPPCs at each end. Bars running in the  $x$  ( $y$ ) directions in the top/bottom (side) modules are 1.52 m (2.36 m) long and are each read by a single MPPC at one end.

The PØD-ECal modules are not intended for  $\pi^0$  reconstruction as this takes place inside the dedicated PØD detector which they surround. However, their presence is required to detect photons

that either do not convert in the active PØD volume or that produce showers only partially contained within the PØD. They can also confirm the passage of charged tracks, identify MIPs, and act as a veto for incoming backgrounds. This allows a simpler construction. Each module is made of six active scintillator layers separated by five layers of 4 mm thick lead converter giving  $3.6 X_0$ . All bars are 2.34 m long and run along the  $z$  direction for all layers. This simplifies construction while meeting the requirements as verified by Monte Carlo simulations. Each bar is read out by a single MPPC at one end.

The Ds-ECal module was constructed in 2008 and was used for beam tests at the CERN T9 PS mixed electron–muon–hadron beam in April–June 2009. It was installed in ND280 in October 2009. The Barrel-ECal and PØD-ECal modules were constructed in 2009–10 and were installed in ND280 in July–October 2010. The complete ECal has been integrated with the rest of ND280 and is taking data.

#### 4.3.6. Side muon range detector (SMRD)

The SMRD performs multiple functions. Firstly, it records muons escaping with high angles with respect to the beam direction and measures their momenta. Secondly, it triggers on cosmic ray muons that enter or penetrate the ND280 detector. Thirdly, it helps identify beam-related event interactions in the surrounding cavity walls and the iron of the magnet.

The SMRD consists of a total of 440 scintillator modules which are inserted in the 1.7 cm air gaps between 4.8 cm thick steel plates which make up the UA1 magnet flux return yokes. The UA1 magnet consists of 16 C-shaped flux return yokes which are grouped in pairs to form a ring surrounding the inner detectors on four sides. Each yoke consists of 16 steel plates and hence has 15 air gaps in the radial direction. Pairs of yokes are labeled 1–8 from upstream to downstream. The SMRD consists of three layers of scintillator modules on the top and bottom for all yokes. Both sides are instrumented with three layers for yokes 1–5, four layers for yoke 6 and six layers for yokes 7 and 8. All of the SMRD modules populate the innermost gaps so as to be able to detect particles escaping the inner detectors. Due to the differently sized spaces for horizontal and vertical gaps, horizontal modules are composed of four scintillation counters with dimensions  $875 \text{ mm} \times 167 \text{ mm} \times 7 \text{ mm}$  (length  $\times$  width  $\times$  height) and vertical modules consist of five scintillation counters with dimensions  $875 \text{ mm} \times 175 \text{ mm} \times 7 \text{ mm}$ . The counter sizes have been optimized to maximize the active area in each magnet gap. The inter-module spacing in the beam direction is determined by the geometry of the inter-yoke spacing. The scintillation counters consist of extruded polystyrene and dimethylacetamide with admixtures of POPOP and paraterphenyl. The surface of each scintillator counter features a white diffuse layer which acts as a reflector. An S-shaped groove, with a bending radius of 2.9 cm and a depth of 2.5 mm which deepens at the counter ends to 4 mm, has been machined into each scintillator in multiple passes to ensure good surface quality. A 1 mm diameter Kuraray Y11 double-clad WLS fiber is glued with Bicon BC600 into each groove [43]. As shown in Fig. 24, the WLS fiber exits both sides of the scintillator through a ferrule which is part of an endcap. The endcaps, which are custom injection molded and made out of black Vectra, are glued and screwed to the end face of each scintillator counter, and were tested to be light-tight at the few photon level.

The outward-facing side of each endcap features a snap-on mechanism which allows for a connector holding a foam spring backed MPPC to couple reliably to the polished WLS fiber ends. The scintillator counters are wrapped in a layer of Tyvek to increase the light yield by about 5%. A stainless steel foil wrapping provides a light-tight and mechanically durable protection layer. Individual SMRD counters are connected into modules by means of aluminum C-channel profiles which are tapered towards the

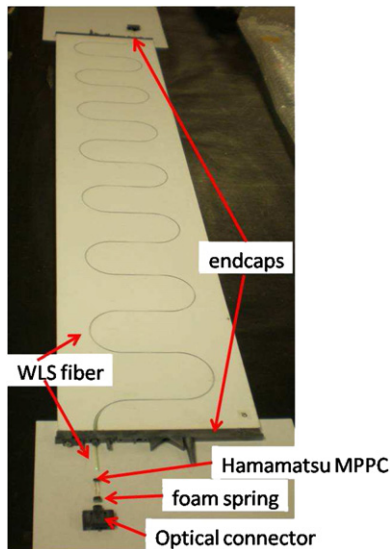


Fig. 24. View of SMRD scintillator counter components prior to assembly.

ends to facilitate installation. Special cut-outs in the C-channels are used as attachment points for bronze springs which serve to center and fix the modules inside the magnet gaps.

All 4016 MPPCs are connected to miniature printed circuit boards (PCBs) which are free to slide along rails in the backside of the optical connector to allow for optimal WLS fiber and MPPC interconnections. The miniature PCBs couple the MPPC signals into mini-coaxial cables, manufactured by Hirose, which lead the signals to the Trip-T front-end boards (TFBs) mounted on the vertical sections of the magnet yokes. The mini-coaxial cables are routed between the magnet yokes and measure 3.5 and 3.0 m for horizontal modules and are 2.2 m long for all vertical modules.

The SMRD front-end electronics consists of 128 TFBs which are described in Section 4.4. Each of the SMRD TFBs features a mezzanine board to connect to and read out up to 12 temperature sensors which are embedded in the scintillator counter endcaps close to the MPPCs. With temperature sensors on both sides of each module, the SMRD supports a network of 880 temperature sensors in total. The TFBs are interconnected via Cat 6 cables to four back-end electronics boards called readout merger modules (RMMs) and two clock trigger modules (CTMs). All of the electronics boards are powered by means of a power distribution system which is mounted along the lower parts of the magnet sides and connected to two Wiener power supply units.

SMRD calibration procedures are shared with other Trip-T based ND280 off-axis subdetectors. The average light yield of individual counters in response to a minimum ionizing particle amounts to about 50 p.e. for the summed signal from both ends of a counter. The beam-related SMRD event rate of coincidence hits has been observed to be stable to within 3% after temperature corrections and a normalization of spills to protons on target (POT) has been applied. The relative timing information of both sensors results in a position resolution of about 7 cm in the direction of the beam. More than one year after construction, the percentage of dead MPPCs in the SMRD is 0.07%.

#### 4.4. ND280 electronics and DAQ

##### 4.4.1. Readout electronics

The PØd, ECal and SMRD subdetectors and the INGRID detector use identical electronics to read out the MPPCs. This electronics is based on the Trip-T ASIC [44]. Signals from 64 MPPCs are routed to custom-designed front-end boards (Trip-T front-end boards or

TFBs) that house four Trip-T ASICs using miniature coaxial cables. The signals from the photosensors are capacitively split (1:10) and routed to two separate channels of the ASIC, to increase the dynamic range of the electronics. Depending on the MPPC gain, a one photoelectron signal corresponds to around 10 ADC counts in the high-gain channel, while the full-scale signal in the low-gain channel corresponds to 500 p.e.

The Trip-T chip integrates the charge in programmable integration windows, which are synchronized with the neutrino beam structure. There is a programmable reset time after each integration cycle, which is at least 50 ns long. The chip can store the result of 23 integration cycles in a capacitor array. Once the 23 integration cycles have been recorded, the data is multiplexed onto two dual-channel 10-bit ADCs, which digitize the data. Signals from the high-gain channel are routed to a discriminator, which is part of the Trip-T ASIC. The front-end board is controlled by an FPGA, which also timestamps the output of the discriminator with an accuracy of 2.5 ns. The discriminator threshold is programmable from 0 to 5 p.e. The ADC and timestamp data is assembled by the FPGA and sent to a back-end board for data concentration and buffering. The output from the discriminators is also used to calculate trigger primitives, which are used to initiate the readout of the detector for cosmic ray muons. Monitoring information (mainly temperature and voltages) is also recorded by the TFB and asynchronously transmitted to the back-end board. More details regarding the front-end part of the electronics can be found in Ref. [45].

The back-end of the electronics system consists of readout merger modules (RMMs), cosmic trigger modules (CTMs), several slave clock modules (SCMs) and a master clock module (MCM). All the boards were developed at the Rutherford Appleton Laboratory using a common hardware platform, which has been built around a high-end Vertex II Pro FPGA from Xilinx, which is clocked at 100 MHz. The board can drive 14 high-speed optical links via its RocketIO and up to 192 LVDS links.

The signals from up to 48 TFBs, which are mounted on the detector and typically less than 1 m away from the photosensors, are routed to one RMM via Cat 5e cables. The RMM controls the TFBs, distributes the clock and trigger signals and receives the data after a trigger signal is received by the TFBs. It sends this data asynchronously via a Gigabit Ethernet link to a commercial PC that collects and processes the data. The RMM is equipped with 500 MB DDR2 memory and can buffer up to 128 triggers. Each RMM receives trigger and timing signals from the SCMs (see below).

The master clock module receives signals from the accelerator that determine when the neutrino spill happens and also from a GPS-based clock. The latter signals are used to synchronize the electronics to UTC. The MCM is also connected to two cosmic trigger modules, which receive signals from up to 192 TFBs or from 48 crate master boards (in the case of the FGD). Based on these signals the CTM will decide whether there was a cosmic event in the detector and trigger the readout. The MCM can also generate pedestal and calibration triggers at a programmable rate. All timing and trigger signals are transmitted via the RocketIO-driven optical link to the slave clock modules. There is one SCM for each of the subdetectors (SMRD, ECal, PØD, FGD, TPC), which allows the electronics to be configured for independent operation of each subsystem. The INGRID is operated independently from ND280 and only uses one MCM and a single CTM. The general layout of the electronics has been visualized in Fig. 25.

##### 4.4.2. DAQ and global slow control

The ND280 data acquisition system has been divided into two components: DAQ and global slow control (GSC). The DAQ

component takes care of the main data stream, collecting the data banks from each subdetector front-end system, storing the data in files and providing online histogramming. The GSC component runs in parallel to the DAQ using the same software framework: MIDAS [27].

The ND280 off-axis and INGRID detectors are equipped with independent DAQ systems which are described in detail in Ref. [46]. These have a common architecture and are based on the MIDAS DAQ framework [27], operating on commercially available computing hardware running the Scientific Linux operating system. MIDAS provides the system with a number of standard components necessary for operation and is interfaced to the experimental hardware through custom C/C++ front-end client applications.

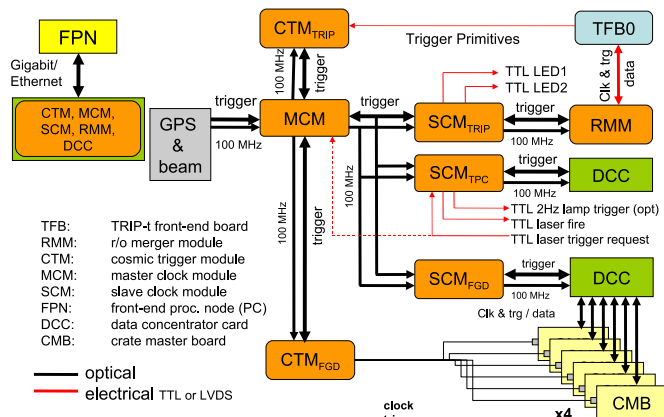


Fig. 25. The general layout of the ND280 electronics.

The system architecture is shown in Fig. 26. In both the INGRID and off-axis systems the back-end electronics modules on the Trip-T-based subdetectors are interfaced to the DAQ by point-to-point optical Gigabit Ethernet links. The MIDAS processes are distributed across a number of nodes to provide the necessary performance and to allow flexible partitioning of the system. An additional MIDAS instance is implemented for each of the FGDs and TPCs in the off-axis detector system. These assemble data from the respective readout electronics and transmit it to the global DAQ. A pair of commercial Gigabit Ethernet switches interconnect the nodes in the DAQ system, providing local infrastructure and data transfer networks. The DAQ networks are isolated from the main T2K experimental network by a further node acting as a gateway.

The Trip-T-based subdetectors are controlled and read out by the front-end processor nodes (FPNs), each of which serves up to two back-end boards. The FPN is implemented as three tasks running as separate processes, interconnected by shared memory data buffers and communicating via standard inter-process mechanisms. Readout and configuration of the electronics and all connected hardware is provided by the readout task (RXT). The readout is parallelized across electronics boards in a multi-threaded manner and data is buffered for access by the data processing task (DPT). The RXT additionally receives periodic monitoring data from the TFBs which it passes to the global slow control. The DPT performs data reduction and basic data processing. It decodes the TFB raw data blocks, associates amplitude and timing information for individual hits, performs pedestal subtraction on a channel-by-channel basis, applies zero suppression to the unsparified data and formats the data for output. To preserve monitoring information, the DPT also performs per-channel histogramming of signal amplitudes for specific trigger types

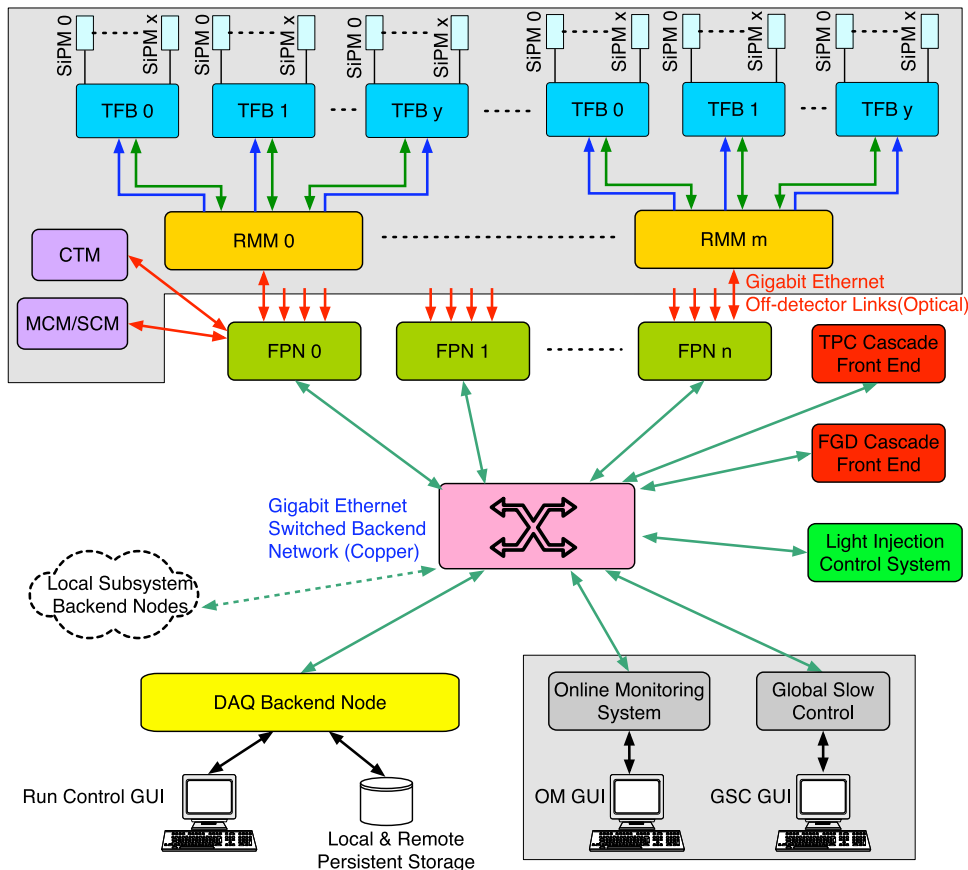


Fig. 26. The architecture of the T2K ND280 off-axis and INGRID detectors' DAQ systems.

prior to zero suppression and periodically inserts the histograms into the output data stream. The processed event fragments are buffered and dispatched to the DAQ back-end by the third process, which implements the MIDAS front-end functionality.

The MIDAS framework provides the core components necessary for the DAQ system and is used to gather the event fragments from the Trip-T FPNs, and the TPC and the FGD front-ends. An event-building process collects the fragments, performs some basic consistency checks and writes the fully assembled events to a system buffer for output to a local RAID array. A custom archiver process transfers completed files to the KEK HPSS [47] mass storage facility over the network and additionally makes a preview copy available to a local semi-offline system for fast-turnaround analysis.

Additional clients are provided to interface the DAQ to the light injection (LI) hardware for the ECal and PØD subdetectors. These configure the LI hardware according to predefined calibration sequences and monitor the status of the LI system. This information is provided in real-time to the DPT, where it is used to manage the formation of calibration histograms. A custom online-monitoring server based around the ROOT framework retrieves built events from the system buffer and generates a range of plots for data and detector quality monitoring.

In terms of hardware, the GSC consists of two PCs and two network switches connecting to subdetector-specific equipment. Front-end tasks running on the GSC PCs or on a subdetector computer connect to the various equipment of the magnet and the subdetectors. A central shared memory database named ODB contains the settings and the readback information from all front-end tasks. This data is in turn stored in a MySQL database at regular intervals. Users interact with the GSC through web pages and can display history plots of any of the stored variables. Several customized web pages have been developed for controlling the magnet, power supplies, electronics parameter settings, and the TPC gas system, or for displaying detector feedback, such as temperature readings or the PØD water target levels. Alarms are set up interactively to catch readback variables going out of range, alerting the shift person as well as sending messages to remote experts. The GSC system is the main tool used by the shift person responsible for safety matters.

The MySQL database containing the GSC information expands at the rate of 0.5 GB per week while taking data. It is an essential element of the calibration process and offline analysis. This database is currently replicated from J-PARC to a server located at TRIUMF. Thanks to this server, collaborators can query the GSC history plots in real-time from a remote location and can connect to the database from computers and grid systems all over the world for data processing.

An electronic logbook (Elog) service is used to complement the GSC system. It runs on a computer in the counting room, with a replica hosted at TRIUMF and is read-write accessible worldwide, with email capabilities. This provides a record of each shift and any maintenance work, and is extremely useful for communication of problems between J-PARC shift people and remote detector experts.

#### 4.5. ND280 software and MC simulation

##### 4.5.1. Introduction

The ND280 offline software suite consists of about 60 software packages totaling over 600,000 lines of original code.

Work on the ND280 offline software commenced in 2004 in order to allow it to be used to aid the early discussions on the design of the ND280 detectors. The design principles that have been followed include an emphasis on the use of standard particle physics software libraries and conventions where possible, structural modularity, good

documentation and openness. Hence ROOT [48] is used for the underlying framework and data storage model, with Geant4 [49] as the basic simulation library. The CMT [50] software configuration management system provides the packaging mechanism, with CVS [51] used to store all versions of the packaging source code files in a repository.

It was anticipated that a large number of physicists, in groups spread across the nations that form the ND280 Collaboration, would write and maintain the software, so a modular structure with well-defined interfaces was chosen such that individual components could be developed independently of each other. Approximately 100 collaborators have actively contributed to the code base as of this writing.

##### 4.5.2. Structure

The general structure of the software suite is indicated in Fig. 27.

The I/O library “oaEvent” defines the file format for the offline software, which is used from the point that the raw MIDAS [27] data files are converted for offline use, up to the production of summarized format files at the end of the chain of processing. It is actively managed to be small and stable. “oaRawEvent” interfaces with the readout data format that is provided by the DAQ group, and allows the raw MIDAS files to be read directly by the offline software. Calibration constants for the detectors are stored on a centralized MySQL database, and are applied by “oaCalib” and its sub-packages at processing time. The access routines for the database are based on those developed for the MINOS experiment.

A representation of the geometry of the detectors is constructed in Geant4 code, and is converted to ROOT TGeoManager [52] format and stored in version-controlled files. These are retrieved from a central repository to be used in the interpretation of raw data.

For Monte Carlo simulations, interfaces have been built between the neutrino beam simulation, the neutrino interaction generation packages, GENIE [53] and NEUT [54] (see Section 5.3), and the ND280 software. The neutrino fluxes estimated from beam MC are passed through the detector geometries, and neutrino cross sections specific to the nuclei present in the geometries are used to generate interactions that are appropriate for the distribution of materials in the detector.

Geant4 is used to simulate the energy deposits from the final state particles that pass through the detector, and the response of the active detectors (scintillator bars, fibers, MPPCs and electronics, and TPC electron drift and electronics) is simulated through custom-written code in the elecSim package.

Individual subdetectors have dedicated packages designed to reconstruct event information internal to them. The RecPack toolkit [55] is used as the framework for event reconstruction

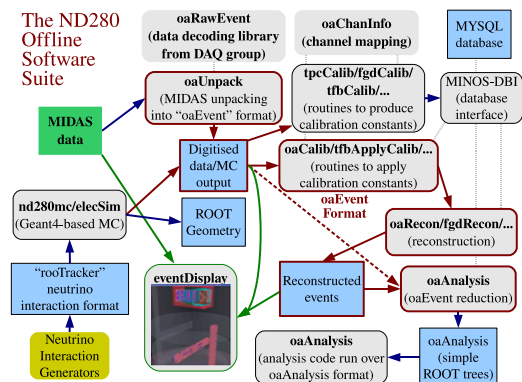
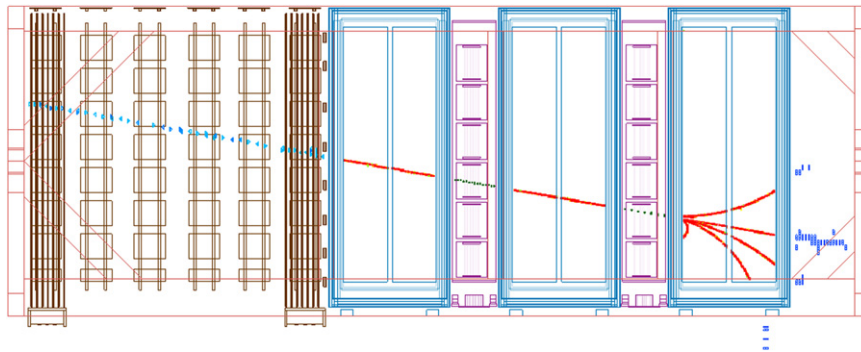


Fig. 27. Schematic of the package structure of the ND280 Software Suite. Only the most representative packages are included.



**Fig. 28.** This event display shows an event with a muon track entering via the front face of the P0D detector, continuing to the tracker (TPC and FGD) region and producing secondary particles on the way. The secondary particles are then stopped in the ECal detectors.

across the off-axis detector. It is an independent software package, but has been developed in close conjunction with the ND280 software to meet its needs.

The full event information contained in the oaEvent format files is distilled by the oaAnalysis package into files based on “trees” which are built up from pure ROOT objects. An accompanying library of analysis tools helps end-users to process the summarized output using standardized C++ routines and Python macros.

An overall software control package allows for the fully automated running of the software, based on simple configuration files which list the inputs and processing steps.

#### 4.5.3. Automated support tools

A number of tools have been used by the ND280 software group to assist in simultaneous code development across a large number of packages. The Buildbot software [56] performs automated builds of the full software suite on multiple computing platforms to test for compilation problems and allow tests to be run. The TUT framework [57] provides a structure for regression tests of code in the low-level packages, to test performance and compliance to specifications. Also, higher-level validation tests were written in multiple packages, to flag problems that are introduced during development.

#### 4.5.4. Management

One individual acts as the release manager, overseeing the packages as they are combined to form “releases” several times a year. In addition to this active management, several tools are used to assist users in contributing to the overall evolution of the software: Bugzilla [58], a widely used management utility for tracking the development of software, allows developers and end-users to file bugs and feature requests; ViewVC [59], a browser-based tool to access all past versions of each file that forms the software suite, tagged with the comments submitted as each change was committed to the repository; and LXR [60], a cross-referenced source code browser.

#### 4.5.5. Documentation

The Doxygen [61] system is used to generate documentation from comments that are embedded in the code. An online workbook is also maintained to provide higher-level documentation on overall procedures and information for new users of the software and developers.

#### 4.5.6. Performance

For the dataset from the first data-taking period in 2010, the neutrino beam events in a single “subrun” file, corresponding to approximately 10 min of data, take approximately 1 h to process fully on a typical CPU.

Fig. 28 shows an event display of an event with a muon track entering into the P0D and continuing into the tracker (TPC and

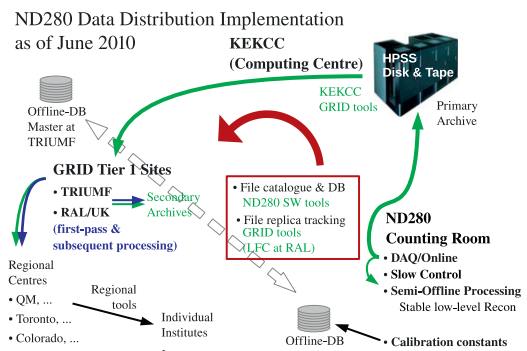


**Fig. 29.** Schematic of the flow of data from the ND280 counting room to the primary and secondary archive sites and the individual collaboration institutions.

FGD) region. Multiple secondary particles are produced in the FGD, all of which are finally stopped in the ECal detectors.

This event display illustrates an overall successful performance of the ND280 off-axis detector system (in terms of both hardware and software).

## 4.6. ND280 data processing and distribution

### 4.6.1. ND280 data

The ND280 detector produces raw data during normal data taking on the order of several MB a second. Single raw data files are approximately 1 GB in size, and are recorded to disk approximately every 10 min. The DAQ group writes these to the HPSS storage system at the KEK Computing Center (KEKCC) as the primary archive for ND280 data.

### 4.6.2. Data distribution

Fig. 29 is a schematic of the flow of data from the ND280 counting room to the end-users, via the primary archive. From the primary archive onwards, tools that were created for the GRID [62] are used to manage the flow and storage of data files. LHC Computing GRID (LCG) utilities are used to transfer files to GRID storage elements at the RAL or TRIUMF laboratories in the U.K. and Canada, respectively, where the data is also copied to long-term storage, for secondary archiving. Once the files are made available on the GRID, they are further distributed to different sites for processing using the LCG tools.

### 4.6.3. Data and Monte Carlo processing

Subsequent processing of these files using the ND280 software suite may be either GRID-based, or based on independent computing clusters with their own batch-processing systems, e.g. SciNet

[63]. Monte Carlo files are generated at computing sites across the collaboration, with different tasks assigned to suit the hardware capabilities of each site. Once these files are generated, they are copied to the GRID, archived at RAL and TRIUMF, and distributed across the collaboration, in the same way as the raw data files.

#### 4.6.4. File cataloging

The procedure described above results in a large number of files, residing on a large number of data storage sites across the international collaborating institutes. Many of these are replicas of each other which are identical in content. These are recorded and tracked using the LCG File Catalog (LFC) tools, which are based around a central catalog for all replica files. This allows end-users to choose a replica that is situated closest to them for working on, or to copy files to a local storage element and register them on the LFC as replicas for subsequent use. Processing jobs can also be sent to locations in which replica files already exist, to minimize the need to transfer data between sites.

## 5. Super-Kamiokande far detector

The world's largest land-based water Cherenkov detector, Super-Kamiokande, serves as the far detector in the T2K experiment. The detector is located 295 km west of the beam source where it is used to sample the beam's flavor composition and look for  $\nu_\mu \rightarrow \nu_e$  appearance and  $\nu_\mu$  disappearance. Built 1 km deep within the center of Mt. Ikenoyama, Super-Kamiokande is a cylindrical cavern filled with 50 kton of pure water within which the detector's roughly 13,000 photomultiplier tubes (PMTs) image neutrino interactions. Super-Kamiokande has been running since 1996 and has produced data for a number of well-known results that include world-leading limits on the proton lifetime [64–66] and the measurement of flavor oscillations in atmospheric, solar and accelerator-produced neutrinos [67–71]. Over this time there have been four running periods: SK-I, SK-II, SK-III, and SK-IV. The latest period, SK-IV, is still in progress and features upgraded PMT readout electronics. SK-IV is also the period in which the T2K experiment takes place.

Because of the detector's long-running operation, the behavior of Super-Kamiokande is well understood. The calibration of the energy scale is known to the percent level, and the software for modeling events in the detector matches calibration samples to the percent level as well.

This section will review the components and operation of Super-Kamiokande, describe the upgraded front-end readout electronics of the detector, and provide an overview of the Monte Carlo simulation of events in Super-Kamiokande. For a much more detailed description of the Super-Kamiokande detector, refer to Ref. [3].

### 5.1. Super-Kamiokande detector overview

The geometry of the Super-Kamiokande detector consists of two major volumes, an inner and an outer detector which are separated by a cylindrical stainless steel structure. Fig. 30 gives a schematic of the Super-Kamiokande detector geometry. The inner detector (ID) is a cylindrical space 33.8 m in diameter and 36.2 m in height which currently houses along its inner walls 11,129 inward-facing 50 cm diameter PMTs. Enclosing the ID is the outer detector (OD) which is a cylindrical space about 2 m thick radially and on the axis at both ends. The OD contains along its inner walls 1,885 outward-facing 20 cm diameter PMTs. The ID and OD boundaries are defined by a cylindrical structure about 50 cm wide. This structure consists of a stainless steel scaffold covered by plastic sheets which serve to optically separate the ID and OD. The wall facing into the ID is lined with a black sheet of plastic meant to absorb light and minimize the number of photons which either scatter off of the ID wall back into the ID volume, or pass through from the ID to the OD. The walls facing the OD, however, are lined with the highly reflective material Tyvek<sup>®</sup>, in order to compensate for the OD's sparse instrumentation. With the Tyvek<sup>®</sup>, photons reflect off of the surface of the OD walls and have a higher chance of finding their way to one of the OD PMTs. Finally, within the stainless steel scaffold there is a 50 cm "dead space", which combines with the ID and OD to make Super-Kamiokande a total of 39 m in diameter and 42 m in height.

The ID is well instrumented, with 40% PMT cathode surface coverage, so that there is sufficient spatial resolution to infer

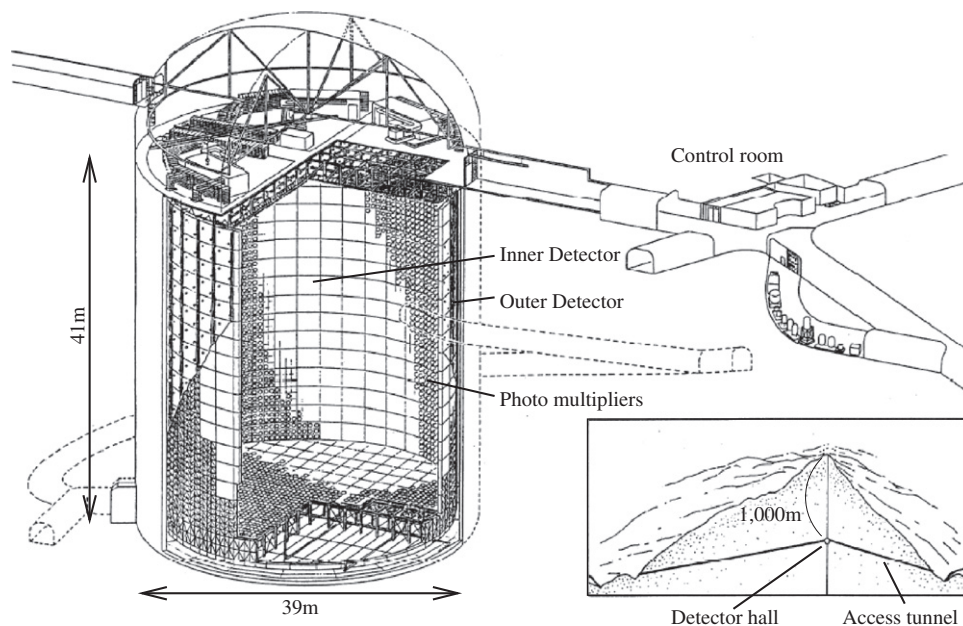


**Fig. 30.** Diagram of the Super-Kamiokande Detector. The detector is mainly comprised of two segments, the inner and outer detectors. The boundary between the two segments is defined by a cylindrical scaffold used to mount photomultiplier tubes and optically separate the segments. The figure comes from Ref. [72].

a number of physical quantities from the imaged neutrino interactions. The ID is lined with Hamamatsu R3600 hemispherical PMTs, which feature a combined quantum and collection efficiency of about 20%. Neutrino interactions often produce charged particles which, if above an energy threshold, produce a cone of Cherenkov photons as they traverse the water. When the photons reach the PMTs on the detector walls they produce a ring-shaped hit pattern which is used to extract information about the interaction such as the event vertex position and momenta of product particles.

The primary strategy to measure the flavor composition of the T2K neutrino beam at Super-Kamiokande, and thereby observe the oscillation of  $\nu_\mu$  to either  $\nu_e$  or  $\nu_\tau$ , is to count charged current quasi-elastic (CCQE) interactions for muon and electron neutrinos, both of which produce leptons of their respective flavor. Muons, counted to measure  $\nu_\mu$  disappearance, are resilient to changes in their momentum due to their relatively large mass. As a result, muons that travel through the detector produce a well-defined cone of Cherenkov radiation which leads to a clear, sharp ring of PMT hits seen on the detector wall. In contrast, electrons, used to search for  $\nu_e$  appearance, scatter more easily because of their smaller mass and almost always induce electromagnetic showers at the energies relevant to Super-Kamiokande. The result of an electron-induced shower is a “fuzzy” ring pattern seen by the PMTs, which can be thought of as the sum of many overlapping Cherenkov light cones. The routines in the Super-Kamiokande event reconstruction software, sketched out in Section 5.3, use this difference between sharp and fuzzy to designate whether the rings imaged in the detector derived from muon-like or electron-like particles.

In contrast to the ID, the OD is only sparsely instrumented due to its original purpose as an active veto of cosmic ray muons and other backgrounds. The PMT array in the OD, made of up 611 Hamamatsu R1408 PMTs and 1274 R5912 PMTs, is capable of an almost 100% rejection efficiency of cosmic ray muon backgrounds. However, by selecting events in coincidence with the T2K beam, neutrino-induced events that illuminate the OD can be efficiently selected from background events. From volume considerations alone, the number of OD events is expected to roughly equal the number of events in the ID. However, because of the OD's narrow geometry and sparse instrumentation, the OD lacks spatial and temporal resolution, which prevents detailed event reconstruction in the OD. Nonetheless, the OD provides a sample of events which can be categorized into three types: events that produced light only in the OD; events where both detector segments are illuminated and the particles seem to originate from an interaction vertex inside the ID; and events where both segments are illuminated but the particles seem to originate from an interaction vertex outside of the ID.

The detector is calibrated through a number of sources, both from introduced laser light and cosmic ray particles.

## 5.2. Super-Kamiokande electronics and DAQ upgrade

In 2008, the Super-Kamiokande collaboration completed an upgrade to the detector's readout electronics [73,74] between the Super-Kamiokande data-taking periods SK-III and SK-IV. This upgrade introduced a new scheme in the acquisition of hits from the detector's 13,014 PMTs. In the old system, once the total number of PMT hits within a 200 ns window exceeded a threshold, a hardware trigger would fire and direct the readout electronics to record data over a specified time window. However, the old front-end's data throughput was too low to accommodate a number of neutrino searches at low threshold, in particular those for solar neutrinos, because the trigger rate at the required threshold level would overload the front-end electronics. The

new upgraded electronics, therefore, includes a new front-end capable of a higher data processing rate. Furthermore, it improves upon the triggering method of the old system. In the new system, the arrival time and charge of each PMT hit is sent to a cluster of PCs that organizes the hit data and searches for event candidates based on programmable software triggers. The new electronics' combination of higher throughput and flexible triggers, along with other improvements such as better impedance matching and a larger front-end dynamic range, improved Super-Kamiokande's ability to better accommodate a larger range of neutrino studies. For example, supernova relic neutrino searches require not only a lower threshold but also a more complicated delayed-coincidence trigger. The new electronics is also capable of implementing a coincidence trigger with a beam arrival time as in the case of the T2K experiment.

The new front-end boards are named QBEE which stands for QTC-based Electronics with Ethernet. The name describes the units at the start and end of the boards' signal processing chain. The QTC (Charge to Time Converter) is a custom ASIC that responds to input PMT pulses by producing a square-wave pulse [75]. The front edge of the QTC's output coincides with the arrival time of the PMT signal and the length is proportional to the integrated charge of the PMT pulse. The output of the QTC is then fed to a TDC (Time to Digital Converter) that digitizes the QTC pulses' times and lengths. Finally, the digitized data from the TDCs is sent to readout PCs using Ethernet technology which provides the needed high rate of data transfer. Custom-made network interface cards, which transfer the data, consist of a TCP/IP firmware, called SiTCP [76], and other interface logic routines that are installed on an FPGA chip. The whole circuit on the QBEE board is able to transfer 11.8 MB/s of data according to a test where analog pulses are sent through the QBEE. This throughput corresponds to an input pulse rate of 80 kHz/channel and is an order of magnitude improvement over the old system which had a maximum hit rate of 1.4 kHz/channel. Each QBEE has eight QTC chips, and the whole DAQ system employs 550 QBEE boards which together read out Super-Kamiokande's 13,014 PMTs and send their hit information to a cluster of online PCs.

The online PCs' role in the DAQ system is to organize the PMT hit information from the QBEEs and produce data files of candidate events which later undergo more offline analysis. The PCs fall into three groups based on their task. The first group consists of 20 “Frontend” PCs. Each PC collects data from 30 ID QBEEs (20 OD QBEEs), and then sorts the PMT hit information in order of time. The second group of PCs, called “Mergers”, collects all hits into a time-ordered list of PMT hits. They also apply a set of software triggers to select event candidates from these lists. There are ten Merger PCs, which each collect data from 30 QBEE boards. For each candidate event, a window is defined around the time of the event trigger and all the information for hits falling within that window is sent to a single “Organizer” PC. The Organizer PC collects all of the candidate events, eliminating overlaps, and writes them to disk for later offline analysis. During a typical period of detector operation, about 470 MB/s of data flows from the Super-Kamiokande PMTs through to the Merger PCs. That stream of hit information results in a software trigger rate of 3 kHz and eventually 9 MB/s worth of candidate event information being written to disk.

For the T2K experiment, the DAQ system was extended to trigger in time with the beam spills produced by the J-PARC accelerator. Each beam spill is given a GPS timestamp that is passed to the online Super-Kamiokande PCs. Each timestamp is used to define an additional software trigger that records all the hit information in a 1 ms window around the T2K beam arrival time. These spill events are then collected and written to disk. Later the events are fed into offline processing which applies the

usual Super-Kamiokande software triggers used to search for neutrino events, and any candidate events found are extracted for further T2K data analysis.

### 5.3. Super-Kamiokande software and MC simulation

The Super-Kamiokande software can be divided into four categories: (1) neutrino event generators, NEUT and GENIE, used to simulate neutrino interactions in the Super-Kamiokande detector, (2) SKDETSIM, which is responsible for modeling Super-Kamiokande's response to particles propagating through the detector, (3) the T2K reduction software which selects neutrino candidate events from detector backgrounds and calibration events, and (4) the Super-Kamiokande event reconstruction library.

#### 5.3.1. NEUT neutrino event generator

The first package, NEUT, produces a list of neutrino interactions and their product particles from a given neutrino flux and energy spectrum. Each interaction NEUT generates is the result of a primary neutrino–nucleon interaction which produces particles that undergo a number of secondary interactions as they propagate out of the nucleus. The primary interactions include quasi-elastic scattering with both free and bound nucleons, single meson production, coherent pion production, and deep inelastic scattering. The secondary interactions are modeled using a particle cascade routine. In the rest of this subsection, a quick overview of the interactions is given. For a more complete description of NEUT, including the details on all of the interactions employed, see Ref. [77].

The cross section for CCQE interactions is computed using one of two different methods depending on whether the scattered nucleon is considered free or bound within a nucleus. For free nucleons, which in the case of water are the protons in hydrogen, the CCQE cross section is calculated using an effective hadronic current and can be found in Ref. [78]. Values for the form factors in the cross section are taken from experimental data [79,80]. For interactions on bound nucleons, NEUT follows the method of Ref. [81] for computing the cross section, in which the momentum distribution of the nucleons is dictated by the Fermi gas model and the outgoing nucleon momentum takes into account Pauli blocking effects. The Pauli blocking model is implemented by requiring that the momentum of the recoiling nucleon be greater than the Fermi surface momentum. This final momentum includes the cost of the nucleon first having to escape the nuclear potential, whose values are from Ref. [82].

NEUT simulates both incoherent and coherent single pion production. Calculation of the incoherent production cross section follows from the method in Ref. [83] in which the decay of baryon resonances produces pions. However, NEUT also uses this method to simulate the production of kaons and etas. The excited resonances are restricted to an invariant mass below 2 GeV, within which pions make up the majority of the outgoing mesons. As for coherent pion production, the calculation of the cross section comes from Ref. [84]. In this interaction, the neutrino can be thought of as interacting with the entire nucleus. The result is an enhancement of pion production in the forward direction, because with the nucleus much heavier than the neutrino most of the incoming momentum is carried away by the outgoing pion.

The deep inelastic scattering (DIS) cross section is computed over an invariant mass energy,  $W$ , greater than 1.3 GeV and employs the nucleon structure functions from GRV98 [85], with corrections suggested by Bodek and Yang. Because a model of single pion production, described above, is already implemented below 2 GeV, the cross-section calculation for  $1.3 \text{ GeV} < W < 2 \text{ GeV}$  only

includes the probability function for pion multiplicities greater than 1 in order to avoid double-counting of this process. The outgoing particles resulting from the DIS interaction are modeled using PYTHIA/JetSet for interactions with  $W$  above 2 GeV and custom-written routines for interactions below 2 GeV. The custom routines were needed because PYTHIA/JetSet was developed for higher energy interactions. For the interactions below 2 GeV, experimental results are used to model the DIS event with KNO scaling employed to interpolate between data points at different values of  $W$  [86].

In addition to the primary interactions above, NEUT models the secondary interactions between the nucleus and any products of the primary interaction, which include mesons and recoiling nucleons. For all of the particles, an initial position of the neutrino interaction in the nucleus is generated in proportion to the Woods–Saxon type nucleon density distribution. From there, a cascade model tracks the initial particle and any of its interaction products out of the nucleus. The interactions during the cascade also include the effects of Fermi motion and Pauli blocking. Of all of the particles, the secondary interactions for pions are the most important due to both the large pion production cross section and the secondary interaction cross sections between the pion and the nucleus. Intranuclear, final state interactions (FSI) of the hadrons produced by the primary neutrino interaction are simulated by a microscopic cascade model. For  $p_\pi < 500 \text{ MeV}/c$ , the mean free paths for quasi-elastic scattering, charge exchange and absorption interaction channels are calculated by Ref. [87], while the scattering kinematics is determined by Ref. [88] with in-medium corrections. For  $p_\pi > 500 \text{ MeV}/c$ , hadron production is also considered, and the mean free paths for all interactions, as well as the scattering kinematics, are determined from fits to pion-proton cross-section data [89]. The model reproduces pion scattering and photoproduction data for nuclei with  $A=12\text{--}209$  [e.g. 90–94]. Secondary interactions for kaons, etas and recoil nucleons are also modeled by a cascade.

#### 5.3.2. GENIE neutrino event generator

GENIE [53] simulates neutrino interactions, for all neutrino flavors and all nuclear targets, over the energy range from a few MeV to several hundred GeV. Over this broad kinematic regime a variety of scattering mechanisms are important.

Charged current quasi-elastic scattering is modeled using an implementation of the Llewellyn-Smith model [78]. The vector form factors are related, via the CVC hypothesis, to electromagnetic form factors measured in electron elastic scattering, with the BBA2005 form factors [95] used by default. The pseudo-scalar form factor in the Llewellyn-Smith model has the form suggested by the PCAC hypothesis [78], while the axial form factor is assumed to have a dipole form. The default quasi-elastic axial vector mass is set to  $0.99 \text{ GeV}/c^2$  [96].

Neutral current elastic scattering is simulated according to the model described by Ahrens et al. [97]. The axial form factor is again assumed to have dipole form with the default axial vector mass set to  $0.99 \text{ GeV}/c^2$ . The factor  $\eta$  accounting for possible isoscalar contributions to the axial current is set to a value of 0.12.

Charged and neutral-current baryon resonance production is described using an implementation of the Rein–Sehgal model [83]. From the 18 baryon resonances of the original paper, GENIE includes the 16 that are listed as unambiguous in the PDG baryon tables [98] and all resonance parameters have been updated. Resonance interference and lepton mass terms are ignored in the cross-section calculation, although lepton mass terms are taken into account in determining the phase space boundaries. The default value of the resonance axial vector mass is  $1.12 \text{ GeV}/c^2$ , as determined from global fits [96].

Charged and neutral-current deep inelastic scattering is described using the effective leading order model of Bodek and Yang [99]. The model provides corrections to be applied on the GRV98 LO parton distributions [85] in order to yield better agreement with low  $Q^2$  electron scattering data. Higher twist and target mass corrections are accounted for through the use of a new scaling variable. The longitudinal structure function is taken into account using the Whitlow parametrization [100]. An overall scale factor of 1.032 is applied to the predictions of the Bodek–Yang model to achieve agreement with the measured value of the neutrino cross section at high energy (100 GeV). The same model is extended in the transition region (hadronic invariant mass below  $1.8 \text{ GeV}/c^2$ ) to simulate non-resonance backgrounds. To avoid double-counting in the transition region, the extrapolated non-resonance background is scaled so that the sum of the resonance and non-resonance contribution fits exclusive one-pion and two-pion cross-section data.

Charged and neutral-current coherent pion production is modeled using an implementation of the Rein–Sehgal model [84]. The model uses the PCAC form at  $Q^2=0$  and assumes a dipole dependence for non-zero  $Q^2$ , with an axial mass of  $1.00 \text{ GeV}/c^2$ . GENIE uses a recent revision of the Rein–Sehgal model [101] where the PCAC formula was updated to take into account lepton mass terms.

Quasi-elastic and deep inelastic charm production is also simulated. Quasi-elastic charm production is simulated using an implementation of Kovalenko’s local duality inspired model [102] tuned to recent NOMAD data [103]. Deep inelastic charm production is modeled according to the Aivazis, Olness and Tung model [104]. Charm production fractions for neutrino interactions are taken from Ref. [105] and the Peterson fragmentation functions are used [106]. The default value of the charm mass is set to  $1.43 \text{ GeV}/c^2$ .

To calculate neutrino cross sections for scattering off nuclear targets, GENIE employs the impulse approximation. The nuclear environment is described using a simple Fermi gas model with a modification by Bodek and Ritchie to include nucleon–nucleon correlations [107].

Neutrino-induced hadronization is simulated using the AGKY model [108]. At low invariant masses, AGKY uses an empirical model anchored to bubble chamber measurements of the average hadronic multiplicity and multiplicity dispersion for neutrino/antineutrino scattering off hydrogen and deuterium. For hadronic invariant masses above  $3 \text{ GeV}/c^2$ , AGKY integrates the PYTHIA-6 fragmentation model [109]. There is a smooth transition between the models to ensure continuity of all simulated observables.

Hadrons produced in the nuclear environment do not immediately re-interact with their full cross section. During the time it takes for quarks to materialize as hadrons, they propagate through the nucleus with a dramatically reduced interaction probability. This is implemented in GENIE using a step during which no re-interaction can occur. The step size is determined from a formation time of  $0.523 \text{ fm}/c$ , according to the SKAT model [110].

Once hadrons are fully formed, the effect of nuclear matter in hadron transport is taken into account using a GENIE sub-package called INTRANUKE [111]. INTRANUKE is an intranuclear cascade MC which tracks pions and nucleons. The hadron re-interaction probability is calculated based on the local density of nucleons [112] and a partial wave analysis of the large body of hadron–nucleon cross sections [89]. Once it has been decided that a hadron re-interacts in the nucleus, the type of interaction is determined based on experimentally measured cross sections. Where data is sparse, cross-section estimates are taken from calculations of the CEM03 group [113]. A number of interaction types are simulated: elastic and inelastic scattering, single charge exchange, and pion production and absorption followed by multi-nucleon knockout.

### 5.3.3. SKDETSIM

The propagation of the particles generated by NEUT across the Super-Kamiokande detector is handled by SKDETSIM, a program library based on the GEANT3 particle propagation package. For hadronic interactions in water, the CALOR physics package is used because of its success at reproducing pion interactions around  $1 \text{ GeV}$  [114]. For pions with momentum below  $500 \text{ MeV}$ , however, custom routines have been written [115]. For the propagation of light in water, SKDETSIM considers absorption, Rayleigh scattering, and Mie scattering as possible interactions. The parameters employed in the model of these processes have been tuned using a number of laser calibration sources.

The overall agreement for SKDETSIM is checked using a number of different cosmic ray samples. For example, the reconstructed momentum spectrum of electrons produced from the decay of cosmic ray muons is compared to the predicted reconstructed spectrum from SKDETSIM. For all samples, the agreement between data and simulation is within a few percent (Fig. 31).

### 5.3.4. T2K data reduction

The T2K reduction software first selects events tagged with the T2K beam trigger from the raw data and then categorizes the beam data into three mutually exclusive samples. Events that are above a certain energy threshold and contain particle tracks that originate and terminate within the ID are labeled as “fully contained”, or FC, events. The number of hits seen in the OD is used to determine whether any particles leave or enter the ID, and so the FC events are required to have no more than 15 hits in the largest OD hit cluster. Those events which exceed this limit are instead categorized as “outer detector”, or OD, events. Events with energy below the FC energy threshold that still display PMT hit patterns suggestive of neutrino interactions, are classified as “low energy”, or LE, events. After categorization, the reduction software then applies a set of cuts unique to each sample to remove backgrounds. The events which pass the cuts are used for physics analyses.

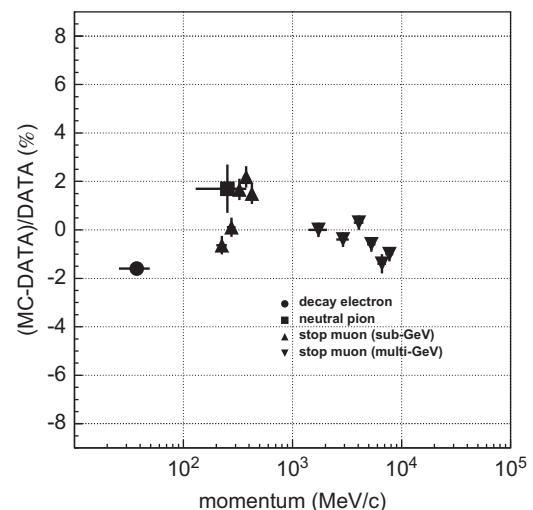


**Fig. 31.** Comparison between data and the SKDETSIM prediction of the reconstructed momentum of different event samples derived from cosmic ray events observed in Super-Kamiokande. For some samples, the comparison is made over different momentum values. “Decay Electron” refers to the reconstructed momentum spectrum of electrons from the decay of cosmic ray muons. “Neutral Pion” is the reconstructed momentum of neutral pions created from atmospheric neutrinos. The “Stop Muon” points indicate the reconstructed momentum of cosmic ray muons which have been determined to stop inside the inner detector.

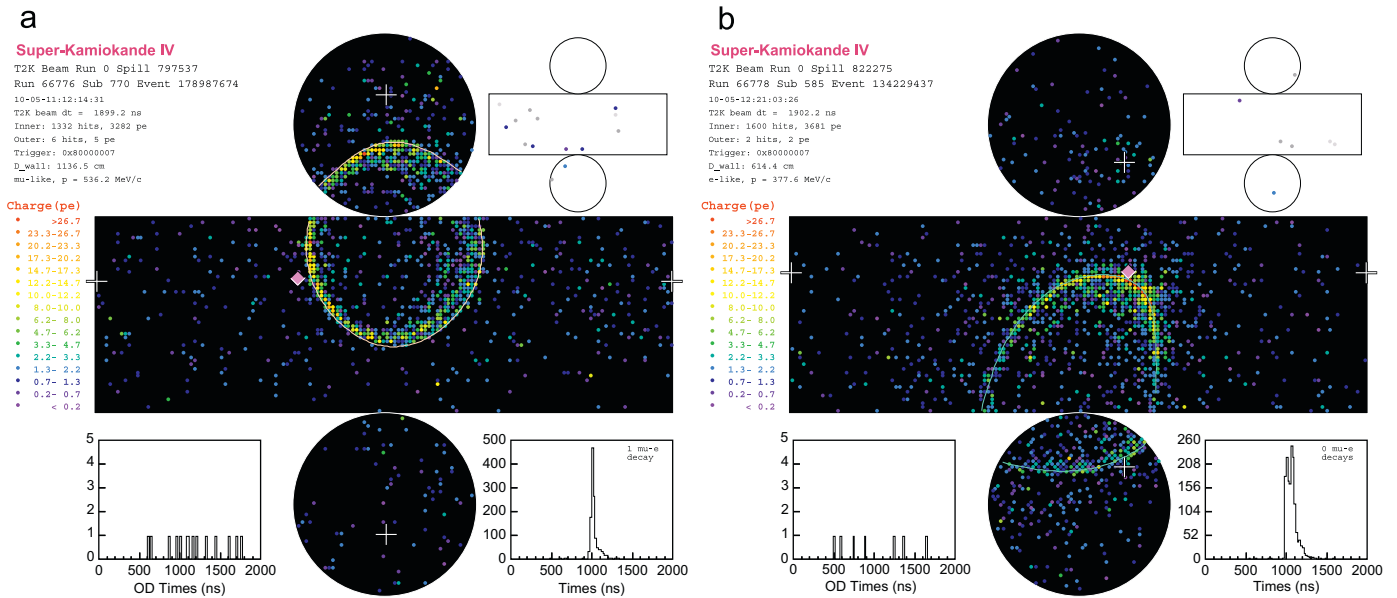


**Fig. 32.** Example of reconstructed T2K events in Super-Kamiokande for (a) a muon-like ring and (b) an electron-like ring. Both figures show the cylindrical detector, unrolled onto a plane. Each colored point represents a PMT, with the color corresponding to the amount of charge, and the reconstructed cone is shown as a white line. The second figure in the upper right corner shows the same hit map for the OD. The white crosses indicate the location of the reconstructed vertex. The diamond marks the location where a ray starting from the event vertex and heading in the direction of the beam would intersect the detector wall. (For interpretation of the references to color in this figure legend, the reader is referred to the web version of this article.)

### 5.3.5. Event reconstruction

The reconstruction of FC and OD events in the detector occurs in four stages. First, an initial event vertex is established from the timing of the PMT hits, and an initial track direction is calculated by searching for a well-defined edge in the PMT charge pattern. Second, an iterative algorithm utilizes a Hough transform of the PMT charge distribution to search for Cherenkov ring candidates. In the third step, a particle identification (PID) algorithm then classifies all the candidate rings observed as either muon-like or electron-like by comparing the observed pattern of charge to an analytically calculated expected pattern in the case of muons and an MC-generated expected pattern in the case of electrons. Finally, the reconstructed momentum for each particle is determined from the distribution of observed charge assigned to the particle's Cherenkov ring. The relationship between the observed charge and the particle's momentum is established using Monte Carlo simulation and detector calibrations from a number of different sources. More details on the event reconstruction algorithm can be found in Ref. [70].

Fig. 32 shows an event display of two T2K neutrino beam interaction events. The left display shows a “muon-like” Cherenkov ring with a sharp outer ring edge, which can be compared to the right display's “electron-like” Cherenkov ring with its characteristic fuzzy edges.

These event displays illustrate an overall successful performance of the Super-Kamiokande detector system (in terms of both hardware and software).

## 6. Conclusion

The T2K experiment, which comprises a new neutrino beamline and new near detector complex at J-PARC and the upgraded Super-Kamiokande detector, has been constructed successfully. The construction of the neutrino beamline started in April 2004. The complete chain of accelerator and neutrino beamline was successfully commissioned during 2009. T2K began accumulating the neutrino beam data for physics analysis in January 2010.

Essentially all components of the experiment perform as expected and there have been no major problems. For example, during the 2010 data taking run, the proportion of good spills for neutrino beams to the total number of spills delivered on target was 99.0%. The overall live times of the INGRID detector, the ND280 off-axis detector system and the Super-Kamiokande detector with regard to the delivered neutrino beam were 99.9%, 96.7% and 99.9%, respectively, demonstrating reliable operation of all of the sub-components of the T2K experiment.

In this paper, we have described the basic structure and parameters of the detector hardware, electronics, online DAQ system, and offline data reduction and distribution scheme. More detailed descriptions of subdetectors can be found in separate papers, some of which have already been published while others are being prepared.

## Acknowledgments

The authors thank the Japanese Ministry of Education, Culture, Sports, Science and Technology (MEXT) for their support for T2K. The T2K neutrino beamline, the ND280 detector and the Super-Kamiokande detector have been built and operated using funds provided by: the MEXT, Japan; the Natural Sciences and Engineering Research Council of Canada, TRIUMF, the Canada Foundation for Innovation, and the National Research Council, Canada; Commissariat à l'Énergie Atomique, and Centre National de la Recherche Scientifique—Institut National de Physique Nucléaire et de Physique des Particules, France; Deutsche Forschungsgemeinschaft, Germany; Istituto Nazionale di Fisica Nucleare, Italy; the Polish Ministry of Science and Higher Education, Poland; the Russian Academy of Sciences, the Russian Foundation for Basic Research, and the Ministry of Education and Science of the Russian Federation, Russia; the National Research Foundation, and the Ministry of Education, Science and Technology of Korea, Korea; Centro Nacional De Física De Partículas, Astropartículas y Nuclear, and Ministerio de Ciencia e Innovación, Spain; the Swiss National Science Foundation and the Swiss State Secretariat

for Education and Research, Switzerland; the Science and Technology Facilities Council, U.K.; and the Department of Energy, U.S.A.

We are also grateful to CERN for their generous donation of the UA1/NOMAD magnet for our use and their assistance with the preparation and operation of the magnet; and to DESY for their generous donation of the HERA-B magnet movers.

In addition, the participation of individual researchers and institutions in the construction of the T2K experiment has been further supported by funds from: the European Research Council; the Japan Society for the Promotion of Science Fellowship for Foreign Researchers program; the U.S. Department of Energy Outstanding Junior Investigator (OJI) Program and Early Career program; and the A. P. Sloan Foundation.

The authors also wish to acknowledge the tremendous support provided by the collaborating institutions, including but not limited to: Ecole Polytechnique—Palaiseau; and the State University of New York at Stony Brook, Office of the Vice President for Research.

## References

- [1] Letter of intent: Neutrino oscillation experiment at JHF, Letter of intent: Neutrino oscillation experiment at JHF, <[http://neutrino.kek.jp/jhfnu/loi/loi\\_JHFcor.pdf](http://neutrino.kek.jp/jhfnu/loi/loi_JHFcor.pdf)>, 2003.
- [2] M. Apollonio, et al., *European Physical Journal C* 27 (2003) 331.
- [3] Y. Fukuda, T. Hayakawa, E. Ichihara, M. Ishitsuka, Y. Itow, et al., *Nuclear Instruments and Methods in Physics Research A* 501 (2003) 418.
- [4] D. Beavis, A. Carroll, I. Chiang, et al., Long Baseline Neutrino Oscillation Experiment at the AGS (Proposal E889), 1995. Physics Design Report, BNL 52459.
- [5] J-PARC TDR, KEK-Report 2002-13 and JAERI-Tech 2003-044, <<http://hadron.kek.jp/accelerator/TDA/tdr2003/index2.html>>, 2003.
- [6] T. Nakamoto, et al., *IEEE Transactions on Applied Superconductivity* 14 (2004) 616.
- [7] T. Nakamoto, et al., An invited paper presented at the 2005 Particle Accelerator Conference (PAC05), Knoxville, Tennessee, USA, 16–20 May 2005.
- [8] T. Ogitsu, et al., *IEEE Transactions on Applied Superconductivity* 15 (2005) 1175.
- [9] T. Okamura, et al., *IEEE Transactions on Applied Superconductivity* 19 (2009) 1125.
- [10] T. Ogitsu, et al., *IEEE Transactions on Applied Superconductivity* 19 (2009) 1081.
- [11] K. Sasaki, et al., *IEEE Transactions on Applied Superconductivity* 20 (2010) 242.
- [12] T. Nakamoto, et al., *IEEE Transactions on Applied Superconductivity* 20 (2010) 208.
- [13] J.-P. Charrier, T2K MSS, <[http://irfu.cea.fr/Phoceia/file.php?class=ast&file=2627/Presentation\\_MES\\_T2K\\_MSS\\_DA.pdf](http://irfu.cea.fr/Phoceia/file.php?class=ast&file=2627/Presentation_MES_T2K_MSS_DA.pdf)>, 2009.
- [14] Toshiba Electron Tubes and Devices Co., Ltd, <<http://www.toshiba-tetd.co.jp/eng/index.htm>>, 2008.
- [15] T. Nakadaira, et al., *AIP Conference Proceedings* 981 (2008) 290.
- [16] S. van der Meer, CERN-61-07, 1961.
- [17] R. B. Palmer, Presented at Informal Conference on Experimental Neutrino Physics, CERN, Geneva, Switzerland, 20–22 January 1965 (C. Franzinetti, (Ed.), CERN-65-32, pp. 141–146).
- [18] K. Matsuoka, et al., *Nuclear Instrumentation and Methods in Physics Research A* 623 (2010) 385.
- [19] K. Matsuoka, et al., *Nuclear Instrumentation and Methods in Physics Research A* 624 (2010) 591.
- [20] T. Nakamura, et al., *Nuclear Instrumentation and Methods in Physics Research A* 556 (2006) 80.
- [21] G.D. Lellis, et al., *Nuclear Instrumentation and Methods in Physics Research A* 512 (2003) 539.
- [22] M. Besnier, Reconstruction and Analysis of Neutrino Interactions in OPERA Target Emulsion Blocks and Discrimination of Charm Background from the Channel  $\tau \rightarrow 3h$ , Ph.D. thesis, Université de Savoie, 2008, LAPP-T-2008-02.
- [23] N. Armenise, et al., *Nuclear Instrumentation and Methods in Physics Research A* 551 (2005) 261.
- [24] I. Kreslo, et al., *Journal of Instrumentation* 3 (2008) P04006.
- [25] T. Higuchi, H. Fujii, M. Ikeno, Y. Igarashi, E. Inoue, et al., TUGT004, 2003.
- [26] H. G. Berns, R. J. Wilkes, FADC board for T2K beam monitors, <[http://neutrino.phys.washington.edu/berns/T2K/ADCCARD/adc2\\_status.html](http://neutrino.phys.washington.edu/berns/T2K/ADCCARD/adc2_status.html)>, <<http://neutrino.phys.washington.edu/berns/T2K/ADCCARD/docs/UWFADC-technote.pdf>>, 2008.
- [27] S. Ritt, P. Amaudruz, K. Olchanski, MIDAS (Maximum Integration Data Acquisition System), <<http://midas.psi.ch>>, 2001.
- [28] M. Clausen, L. Dalesio, ICFA Beam Dynamics Newsletter 47 (2008) 56.
- [29] SAD, Strategic accelerator design, Developed in KEK, <<http://acc-physics.kek.jp/SAD/>>, 1986.
- [30] N. Abgrall, et al., Report from the NA61/SHINE experiment at the CERN SPS, Technical Report CERN-SPSC-2010-025. SPSC-SR-066, CERN, Geneva, 2010.
- [31] N. Abgrall, et al., Measurements of Cross Sections and Charged Pion Spectra in Proton–Carbon Interactions at 31 GeV/c, 2011. Preprint: CERN-PH-EP-2011-005.
- [32] FLUKA version 2008.3c, <<http://www.fluka.org/fluka.php>, 2008>.
- [33] GEANT3, A detector description and simulation tool, Application Software Group, Computing and Networks Division, CERN, Geneva, 1993.
- [34] D. Renker, E. Lorenz, *Journal of Instrumentation* 4 (2009) P04004.
- [35] M. Yokoyama, et al., *Nuclear Instruments and Methods in Physics Research A* 610 (2009) 128.
- [36] M. Yokoyama, et al., *Nuclear Instruments and Methods in Physics Research A* 622 (2010) 567.
- [37] A. Vacheret, G. Barker, M. Dziejewski, P. Guzowski, M. Haigh, et al., *Nuclear Instruments and Methods in Physics Research A*, 2011. Preprint: arXiv1101.1996.
- [38] A. Pla-Dalmau, *Frascati Physics Series* 21 (2001) 513.
- [39] F. Moreau, et al., *Nuclear Instruments and Methods in Physics Research A* 613 (2010) 46.
- [40] A. Pla-Dalmau, A. Bross, V. Rykalin, B. Wood, *Nuclear Science Symposium Conference Record* 3 (2005) 1298.
- [41] I. Giomataris, et al., *Nuclear Instruments and Methods in Physics Research A* 560 (2006) 405.
- [42] N. Abgrall, B. Andrieu, P. Baron, P. Bene, V. Berardi, et al., *Nuclear Instruments and Methods in Physics Research A* 637 (2011) 25.
- [43] A. Izmaylov, et al., *Nuclear Instruments and Methods in Physics Research A* 623 (2010) 382.
- [44] L. Bellantoni, P. Rubinov, Bench test of first Trip-T prototypes, DO note 4845 <<https://plone4.fnal.gov/P1/AFEIUpgrade/tript/>>, 2005.
- [45] A. Vacheret, S. Greenwood, M. Noy, M. Raymond, A. Weber, in: *Nuclear Science Symposium Conference Record*, 2007, NSS '07. IEEE, vol. 3, pp. 1984–1991.
- [46] M. Thorpe, et al., in: *Proceedings of the 17th IEEE Real Time Conference*, 2010, doi:10.1109/RTC.2010.5750358.
- [47] T. H. Collaboration, High Performance Storage System (HPSS), <<http://hpss-collaboration.org>>, 2010.
- [48] R. Brun, F. Rademakers, *Nuclear Instruments and Methods in Physics Research A* 389 (1997) 81.
- [49] S. Agostinelli, et al., *Nuclear Instruments and Methods in Physics Research A* 506 (2003) 250.
- [50] C. Arnault, in: *Prepared for International Conference on Computing in High-Energy Physics and Nuclear Physics (CHEP 2000)*, Padova, Italy, 7–11 February 2000.
- [51] B. Berliner, J. Polk, *Concurrent Versions Systems (CVS)*, <<http://www.cvshome.org>>, 2001.
- [52] R. Brun, A. Gheata, M. Gheata, *Nuclear Instruments and Methods in Physics Research A* 502 (2003) 676.
- [53] C. Andreopoulos, et al., *Nuclear Instruments and Methods in Physics Research A* 614 (2010) 87.
- [54] Y. Hayato, *Acta Physica Polonica B* 40 (2009) 2477.
- [55] A. Cervera-Villanueva, J.J. Gomez-Cadenas, J.A. Hernando, *Nuclear Instruments and Methods in Physics Research A* 534 (2004) 180.
- [56] B. Warner, D. Mitchell, Buildbot, <<http://buildbot.net>>, 2010.
- [57] V. Dyuzhev, D. Kononenko, M. Rzechonek, TUT: C++ template unit test framework, <<http://tut-framework.sourceforge.net>>, 2009.
- [58] T. Weissman, et al., Bugzilla Defect Tracking System, <<http://www.bugzilla.org>>, 2010.
- [59] B. Fenner, H. Zeller, et al., ViewVC: Web-based version control repository browsing, <<http://www.viewvc.org>>, 2005.
- [60] A. G. Gleditsch, LXR Cross Referencer, <<http://sourceforge.net/projects/lxr>>, 2010.
- [61] D. van Heesch, Doxygen, <<http://www.stack.nl/dimitri/doxygen/>>, 2010.
- [62] I. Bird (Ed.), et al., CERN-LHCC-2005-024, 2005.
- [63] C. Loken, D. Gruner, et al., *Journal of Physics: Conference Series* 256 (2010) 012026.
- [64] M. Shiozawa, et al., *Physical Review Letters* 81 (1998) 3319.
- [65] Y. Hayato, et al., *Physical Review Letters* 83 (1999) 1529.
- [66] H. Nishino, et al., *Physical Review Letters* 102 (2009) 141801.
- [67] Y. Fukuda, et al., *Physical Review Letters* 81 (1998) 1562.
- [68] Y. Fukuda, et al., *Physical Review Letters* 82 (1999) 2430.
- [69] M. Ahn, et al., *Physical Review D* 74 (2006) 072003.
- [70] Y. Ashie, et al., *Physical Review D* 71 (2005) 112005.
- [71] J. Hosaka, et al., *Physical Review D* 74 (2006) 032002.
- [72] Y. Itow, et al., The JHF-Kamioka neutrino project, arxivhep-ex/0106019, 2001.
- [73] H. Nishino, et al., in: *Nuclear Science Symposium Conference Record*, 2007, NSS'07, IEEE, vol. 1, 2008, p. 127.
- [74] S. Yamada, et al., in: *16th IEEE-NPSS Real Time Conference Proceedings*, 2009, p. 201.
- [75] H. Nishino, K. Awai, Y. Hayato, S. Nakayama, K. Okumura, et al., *Nuclear Instruments and Methods in Physics Research A* 610 (2009) 710.
- [76] T. Uchida, M. Tanaka, in: *Nuclear Science Symposium Conference Record*, 2006, IEEE, vol. 3, 2006, p. 1411.
- [77] Y. Hayato, *Nuclear Physics B—Proceedings Supplements* 112 (2002) 171.
- [78] C. Llewellyn Smith, *Physics Report* 3 (1972) 261.
- [79] H. Grabosch, et al., *Zeitschrift für Physik C* 41 (1989) 527.

- [80] V. Bernard, L. Elouadrhiri, U. Meissner, *Journal of Physics G Nuclear Physics* 28 (2002) R1.
- [81] R. Smith, E. Moniz, *Nuclear Physics B—Proceedings Supplements* 43 (1972) 605.
- [82] F. Brieva, A. Dellafiore, *Nuclear Physics A* 292 (1977) 445.
- [83] D. Rein, L.M. Sehgal, *Annals of Physics* 133 (1981) 79.
- [84] D. Rein, L.M. Sehgal, *Nuclear Physics B—Proceedings Supplements* 223 (1983) 29.
- [85] M. Gluck, E. Reya, A. Vogt, *European Physical Journal C* 5 (1998) 461.
- [86] H. Saarikko, Presented at Neutrino '79, Bergen, Norway, 1979.
- [87] L. Salcedo, E. Oset, M. Vicente-Vacas, C. Garcia-Recio, *Nuclear Physics A* 484 (1988) 557.
- [88] G. Rowe, M. Salomon, R.H. Landau, *Physical Review C* 18 (1978) 584.
- [89] R.A. Arndt, W.J. Briscoe, I.I. Strakovsky, R.L. Workman, M.M. Pavan, *Physical Review C* 69 (2004) 035213.
- [90] T. Lee, R. Redwine, *Annual Review of Nuclear and Particle Science* 52 (2002) 23.
- [91] D. Ashery, I. Navon, G. Azuelos, H. Walter, H. Pfeiffer, et al., *Physical Review C* 23 (1981) 2173.
- [92] C. Ingram, P. Gram, J. Jansen, R. Mischke, J. Zichy, et al., *Physical Review C* 27 (1983) 1578.
- [93] B. Allardyce, C. Batty, D. Baugh, E. Friedman, G. Heymann, et al., *Nuclear Physics A* 209 (1973).
- [94] J. Arends, J. Eyink, H. Hartmann, A. Hegerath, B. Mecking, et al., *Zeitschrift für Physik A* 305 (1982) 205.
- [95] R. Bradford, A. Bodek, H.S. Budd, J. Arrington, *Nuclear Physics Proceedings Supplementary* 159 (2006) 127.
- [96] K.S. Kuzmin, V.V. Lyubushkin, V.A. Naumov, *Acta Physica Polonica B* 37 (2006) 2337.
- [97] L.A. Ahrens, et al., *Physical Review D* 35 (1987) 785.
- [98] W.M. Yao, et al., *Journal of Physics G Nuclear and Particle Physics* 33 (2006) 1.
- [99] A. Bodek, U.K. Yang, *Journal of Physics G Nuclear and Particle Physics* 29 (2003) 1899.
- [100] L.W. Whitlow, S. Rock, A. Bodek, E.M. Riordan, S. Dasu, *Physics Letter B* 250 (1990) 193.
- [101] D. Rein, L.M. Sehgal, *Physics Letters B* 657 (2007) 207.
- [102] S.G. Kovalenko, *Soviet Journal of Nuclear Physics* 52 (1990) 934.
- [103] M. Bischofberger, Quasi Elastic Charm production in Neutrino Nucleon Scattering, Ph.D. thesis, Eidgenössische Technische Hochschule Zuerich, Switzerland, 2005.
- [104] M.A.G. Aivazis, F.I. Olness, W.-K. Tung, *Physical Review D* 50 (1994) 3085.
- [105] G. De Lellis, F. Di Capua, P. Migliozi, *Physics Letters B* 550 (2002) 16.
- [106] C. Peterson, D. Schlatter, I. Schmitt, P.M. Zerwas, *Physical Review D* 27 (1983) 105.
- [107] A. Bodek, J.L. Ritchie, *Physical Review D* 24 (1981) 1400.
- [108] T. Yang, C. Andreopoulos, H. Gallagher, K. Hoffmann, P. Kehayias, *European Physical Journal C* 63 (2009) 1.
- [109] T. Sjostrand, et al., *Computer Physics Communications* 135 (2001) 238.
- [110] D. Baranov, V. Ermolaev, A. Ivanilov, P. Ivanov, V. Hleborad, et al., *PHE* 84-04, 1984.
- [111] S. Dytman, *Acta Physica Polonica B* 40 (2009) 2445.
- [112] H. De Vries, C.W. De Jager, C. De Vries, *Atomic Data and Nuclear Data Tables* 36 (1987) 495.
- [113] S.G. Mashnik, A.J. Sierk, K.K. Gudima, M.I. Baznat, *Journal of Physics Conference Series* 41 (2006) 340.
- [114] C. Zeitnitz, T. Gabriel, *Nuclear Instruments and Methods in Physics Research A* 349 (1994) 106.
- [115] M. Nakahata, et al., *Journal of the Physical Society of Japan* 55 (1986) 3786.